AD-A141 246

NITRAMINE PROPELLANT CRACK TIP IGNITION AND CRACK
PROPAGATION OF A BURNING SAMPLE UNDER RAPID
PRESSURIZATION

SUMMARY REPORT

Prepared by
K. K. Kuo, J. G. Siefert, J. Mantzaras,
W. H. Hsieh, and F. Koo

October 1983

20000803082

THE PENNSYLVANIA STATE UNIVERSITY
College of Engineering
Department of Mechanical Engineering
University Park, Pennsylvania

84 05 17 053

REPORT DOCUMENTATION PAGE		READ INSTRUCTIONS BEFORE COMPLETING FORM
1. REPORT NUMBER	2. GOVT ACCESSION NO. $AD \cdot A141246$	3. RECIPIENT'S CATALOG NUMBER
4. TITLE (and Subtitle) NITRAMINE PROPELLANT CRACK TIP IGNITION AND CRACK PROPAGATION OF A BURNING SAMPLE UNDER RAPID PRESSURIZATION		5. TYPE OF REPORT & PERIOD COVERED Summary Sept. 1, 1982 – Aug. 31, 1983
		6. PERFORMING ORG. REPORT NUMBER
7. AUTHOR(s) K. K. Kuo, J. G. Siefert, J. Mantzaras, W. H. Hsieh, and F. Koo		8. CONTRACT OR GRANT NUMBER(s) N00014-79-C-0762
9. PERFORMING ORGANIZATION NAME AND ADDRESS Department of Mechanical Engineering The Pennsylvania State University University Park, PA 16802		10. PROGRAM ELEMENT, PROJECT, TASK AREA & WORK UNIT NUMBERS
11. CONTROLLING OFFICE NAME AND ADDRESS Office of Naval Research Power Program Arlington, Va. 22217		12. REPORT DATE Nov. 1983
		13. NUMBER OF PAGES
14. MONITORING AGENCY NAME & ADDRESS(if different from Controlling Office)		15. SECURITY CLASS. (of this report) Unclassified
		15a. DECLASSIFICATION/DOWNGRADING SCHEDULE

16. DISTRIBUTION STATEMENT (of this Report)

Approved for public release; distribution unlimited

17. DISTRIBUTION STATEMENT (of the abstract entered in Block 20, if different from Report)

18. SUPPLEMENTARY NOTES

19. KEY WORDS (Continue on reverse side if necessary and identify by block number)

Ignition, Deflagration-to-Detonation Transition, Crack Propagation, AP-Composite Propellant, Ignition Delay, Stagnation Point Heat Transfer, Microstructure Damage, Crack Branching, Finite Element Stress Analysis, Nitramine Propellants

20. ABSTRACT (Continue on reverse side if necessary and identify by block number)

(see next page)

DD FORM 1 JAN 73 1473

ii

ABSTRACT

Two major tasks performed during the report period of investigation were: (i) crack tip ignition phenomena under rapid pressurization and (ii) crack propagation in burning solid propellants.

Ignition of nitramine composite propellants located at the tip of an inert crack was investigated both experimentally and theoretically. A theoretical model is proposed for the ignition of nitramine composite propellants. Specific features considered in the model include: a) detailed chemical kinetics information for the ignition of nitramine composite propellants, b) two-dimensional (axisymmetric) geometry for the composite propellant, and c) rapid pressurization of the gas phase simulating actual rocket motor ignition conditions. The ignition process was also observed by simultaneously using a high-speed movie camera, a fast-response photodiode system, and a near-infrared photodiode system. Many nitramine propellants showed momentary ignition followed by extinction. It is found that the time required for the onset of gas evolution of nitramine propellants decreases as the pressurization rate is increased. Under the same operating conditions, nitramine-based composite propellants are harder to ignite than AP-based propellants. Nitramine propellants with HMX fillers are slightly more difficult to ignite than RDX-based propellants due to higher thermal diffusivity and activation energy for decomposition.

Mechanism of crack propagation in a burning composite propellant subjected to rapid pressurization (up to 30 GPa/s) was investigated experimentally. A visual record of the event was made using a high-speed movie camera. The effect of pressurization rate on crack propagation velocity, the mass burning rate, and time variation of crack shape was studied. Experimental results indicate that the mass burning rate and the propagation velocity of the luminous front increases as the pressurization rate is increased. For high pressurization rates in the order of 10 GPa/s, the luminous crack tip contour undergoes a highly discernible transition process that a triangular contour develops into a mushroom-shaped region. The evolution of the mushroom-shaped region is believed to be caused by gas penetration and flame propagation into micropores resulting from crack branching. The mass burning rate deduced from a mass balance in the chamber using measured chamber p-t trace is nearly two orders of magnitude higher than that based upon steady-state burning rate. This substantial increase in the mass burning rate is believed to be caused by the additional burning surface area created by microstructure damage. Dynamic burning effect could also be a contributing factor. The observed crack propagation phenomena and enhanced mass burning rate may play an important part in the DDT process.

NITRAMINE PROPELLANT CRACK TIP IGNITION AND CRACK PROPAGATION
OF A BURNING SAMPLE UNDER RAPID PRESSURIZATION

SUMMARY REPORT

Sponsored by

Office of Naval Research
Power Program
Arlington, Virginia

Contract No. N00014-79-C-0762

Prepared by

Kenneth K. Kuo
John G. Siefert
John Mantzaras
W. H. Hsieh
Francis Koo

Department of Mechanical Engineering
The Pennsylvania State University
University Park, PA 16802

Reproduction in whole or in part is permitted for
any purpose of the United States Government.

Approved for public release; distribution unlimited

ACKNOWLEDGEMENT

TABLE OF CONTENTS

LIST OF FIGURES

LIST OF TABLES

NOMENCLATURE

A_t area of exit nozzle, m^2

c, c_p specific heat, kJ/kg.K

$\mathcal{D}$ binary mass diffusion coefficient, m^2/s

E activation energy, J/kmole

G external radiation heat flux, kW/m^2

k thermal conductivity, kW/m.K

k_i rate constants for reaction i

L thickness of oxidizer pellet, m

m_b apparent mass burning rate of propellant, kg/s

$m_{b,ss}$ steady-state mass buring rate of propellant, kg/s

m_{in} mass flow rate into the chamber, kg/s

m_{out} mass flow rate out of the chamber, kg/s

P pressure, MPa

$\dot{q}''$ heat flux (energy per unit time per unit area), kW/m^2

$\dot{q}'''$ heat generation rate, kW/m^3

Q_{py} heat of pyrolysis per unit mass, kJ/Kg

r radial distance from center of statistically averaged element, m

r_b burning rate, m/s

R gas constant, kJ/Kg.K

R_u universal gas constant, kJ/kmole.K

R_1, R_2 radii of outer surfaces of oxidizer particle and fuel binder, respectively, m

s displacement, m

t time, s

T	temperature, K
V_c	crack propagation velocity, m/s
v_z	gas phase velocity in z direction, m/s
W	average molecular weight, kg/kmole
Y_j	mass fraction of species j in gas phase
z	distance from initial (t=0) position of interface; positive in gas phase, m
Z	pre-exponential factor, 1/s or m^3/kmole.s or kg/m^2.s
α	radiation absorptivity of interface
β	in-depth radiation absorption coefficient, 1/m
γ	ratio of specific heats
ρ	density, kg/m^3
τ	transmissivity of solid phase
$\dot{\omega}''$	mass production rate per unit area, kg/m^2
$\dot{\omega}'''_i$	mass production rate per unit volume, kg/m^3

Subscripts

1,2,3,4,5	various reactions or species
c or ch	chamber
F	fuel
g	gas-phase
i	initial value or species i
Ox	oxidizer
Ox-F	oxidizer-fuel interface
py	pyrolysis
s	solid phase
s-g	solid-gas interface

I. INTRODUCTION

This report summarizes progress made during the period September 1, 1982 to August 31, 1983, under the project entitled "Ignition of Solid Propellants and Propagation of Burning Propellant Cracks" (Contract No. N00014-79-C-0762).

The overall objective of this investigation is to achieve better under-standing of the ignition mechanism under transient pressure loading conditions and to investigate propagation of burning solid propellant cracks. Specific objectives of this study are:

1. to observe the ignition phenomena of nitramine composite propellants, and to measure ignition delay under various operating conditions;

2. to compare ignition delays of different types of propellant samples under identical flow conditions;

3. to study the effect of binder and oxidizer ingredients on ignition by comparing the ignition processes of propellants with different ingredients;

4. to propose a theoretical model for the ignition of nitramine propellants, and to gain a deeper understanding of the ignition process;

5. to observe crack propagation phenomena in burning solid propellant samples;

6. to study the mechanism of crack propagation and branching;

7. to determine the effect of pressurization rate and sample geometry on crack propagation velocity; and

8. to evaluate the ratio of effective mass burning rate to the steady-state mass burning rate of the sample under various operating conditions.

The following is a list of papers published during the past year under the support of this contract.

1. "Ignition of Composite Propellants in a Stagration Region Under Rapid Pressure Loading," Nineteenth International Symposium on Combustion, The Combustion Institute, 1982, pp. 757-767 by M. Kumar, J. E. Wills, A. K. Kulkarni, and K. K. Kuo.

2. "Ignition of Nitramine Propellants Under Rapid Pressurization," AIAA/SAE/ASME 19th Joint Propulsion Conference, AIAA Paper 83-1194, Seattle, Washington, June 27-29, 1983 by S. Yu, W. H. Hsieh and K. K. Kuo.

3. "Mechanism of Crack Propagation in Burning Solid Propellants," 1983 JANNAF Propulsion Systems Hazards Meeting, Los Alamos, NM, July 13-15, 1983 by K. K. Kuo, J. G. Siefert, M. Kumar, W. H. Hsieh, and E. Andiroglu.

4. "Crack Propagation in Burning Solid Propellants," The Proceedings of the Ninth International Colloquium on the Dynamics of Explosions and Reactive Systems, Poitiers, France, July 3-8, 1983 by J. G. Siefert and K. K. Kuo.

5. "Nitramine Propellant Ignition Under Rapid Gas Loading Conditions," 20th JANNAF Combustion Meeting, Monterey, California, Oct. 17-20, 1983 by S. Yu, W. H. Hsieh, and K. K. Kuo.

Besides the above publications, research results obtained from this project were also presented at the following workshops.

1. "Ignition of Nitramine-LOVA Propellants," presented at the JANNAF Workshop on Characteristics of Nitramine-LOVA Gun Propellants held at NOS, Indian Head, MD, June 14-15, 1983 by K. K. Kuo, S. Yu, and W. H. Hsieh.

2. "Crack Propagation in Burning Solid Propellants," presented in ONR Workshop on Dynamic Deformation, Fracture and Transient Combustion, held at Chestertown, MD, July 28-29, 1983 by K. K. Kuo.

II.   INVESTIGATION OF COMPOSITE PROPELLANT IGNITION MODEL

2.1 Brief Introduction of Nitramine Propellant Ignition

A fundamental understanding of the ignition process of nitramine solid propellants is important to the design of rocket motors and artillery propulsion systems. Most of the solid propellant ignition studies were performed on AP-based composite propellants and homogeneous propellants. A detailed review of literature on solid propellant ignition was conducted by Price et al.,[1] and more recently by Hermance[2], and Kulkarni, Kumar, and Kuo.[3] Ignition of traditional AP-based composite solid propellants located at the tip of an inert crack was investigated both experimentally and theoretically by Kuo and coworkers.[4-7] A comprehensive model[7] and numerical solutions for ignition of AP-based composite solid propellants under rapid pressurization rate were presented. The rapid pressurization situation is typical of ignition transients in rocket motors and the onset of deflagration-to-detonation transition (DDT) in confined, damaged propellant grains.

The use of nitramine oxidizer in composite propellants has become of great interest because it offers many advantages in rocket and gun propulsion. High specific impulse is obtained due to the combination of high energy and low molecular weight of product gases.[8,9] The excellent thermal stability of HMX and RDX makes nitramine composite propellants the best candidate for Low Vulnerability Ammunition (LOVA) propellants.[10,11] In addition, replacement of the currently used AP oxidizer by HMX or RDX oxidizer eliminates HCl in the exhaust gases and reduces secondary smoke due to nucleation of moisture to form droplets.

In the ignition of nitramine propellants, experimental work conducted by DeLuca, Caveny, Ohlemiller, and Summerfield[12,13] showed that HMX composite propellants are more difficult to ignite by arc-image furnace or CO_2 laser than AP-based composite propellants and noncatalyzed double-base propellants. Similar results obtained by Birk and Caveny[14] also showed that HMX composite propellants are more difficult to ignite under transient flow conditions than single-base, double-base, and triple-base propellants. In spite of these studies, the ignition process of nitramine propellants under rapid pressurization situation has not been studied thoroughly.

2.2 Theoretical Approach

2.2.1 Description of Physical Model

The physical processes that lead to ignition are as follows. Hot combustion product gases from the igniter or main chamber flow into the crack cavity and pressurize it. This causes the pressure of the gases adjacent to the propellant surface to increase rapidly. As the process continues, energy is transferred from the hot gases to the propellant. Following a period of inert heating, the propellant starts to decompose. The fuel and oxidizer species evolved from the surface diffuse and mix with the surrounding gases. In the gas phase, oxidizer species react with the fuel species; at the same time, surface and/or subsurface reactions in the solid phase continue. When the net heat evolved from chemical reactions overcomes the heat losses, the temperatures start to rise. Eventually, ignition characterized by a high rate of chemical reactions and heat release, is achieved.

The physical model considers an oxidizer particle embedded in a fuel binder matrix. In an actual composite propellant, oxidizer particles of

random size (within a certain range) are distributed in a fuel binder. Figure 1 shows typical side cross-section and top views of a typical unimodel composite propellant. Following Ref. 7 in the mathematical simulation of this type of propellant, the shape of the oxidizer particles is approximated by a cylindrical pellet of radius R_1, and thickness L, enveloped by a fuel binder of radius R_2 as shown in Fig. 2. A two-dimensional geometry closely represents a composite propellant, while being mathematically tractable. The gas-phase pressure-time (P-t) relationship is assumed to be known either from a measured P-t trace, or a prescribed P-t information simulating a given operating condition. Because pressure is not usually extremely high during the ignition interval, the perfect gas law can be used as the equation of state.

2.2.2 Governing Equations

For the coordinates shown in Fig. 2, heat equations for the oxidizer and fuel binder in the solid phase are

$$\text{Oxidizer:} \quad \rho_{Ox,s} c_{Ox,s} \frac{\partial T}{\partial t} = \frac{\partial}{\partial z}\left(k_{Ox,s} \frac{\partial T}{\partial z}\right) + \frac{1}{r}\frac{\partial}{\partial r}\left(k_{Ox,s} r \frac{\partial T}{\partial r}\right)$$
$$+ \dot{q}'''_{Ox,s} \tag{1}$$

$$\text{Fuel:} \quad \rho_{F,s} c_{F,s} \frac{\partial T}{\partial t} = \frac{\partial}{\partial z}\left(k_{F,s} \frac{\partial T}{\partial z}\right) + \frac{1}{r}\frac{\partial}{\partial r}\left(k_{F,s} r \frac{\partial T}{\partial r}\right)$$
$$+ \dot{q}'''_{F,s} \tag{2}$$

where

$$\dot{q}'''_{Ox,s} = \dot{q}'''_{Ox,\,radiation} + \dot{q}'''_{Ox,pyrolysis} \tag{3}$$

CROSS-SECTIONAL VIEW   TOP VIEW

OXIDIZER
PARTICLE

FUEL BINDER

A TYPICAL ELEMENT
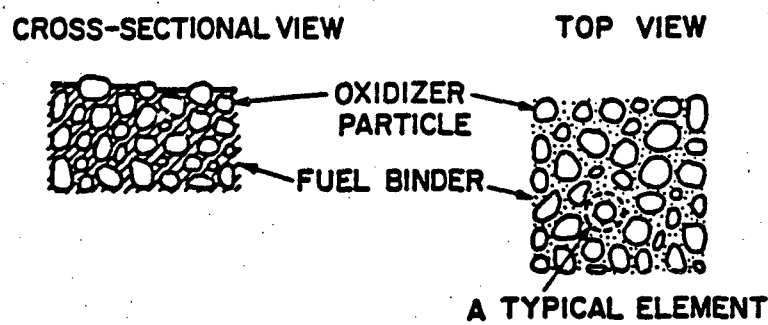
Fig. 1 Heterogeneous Structure of Nitramine
Composite Propellants

IGNITER GAS

GAS PHASE

$z(I)$

$r(J)$

L

OXIDIZER

R_1

R_2

FUEL BINDER

ADIABATIC
BOUNDARIES
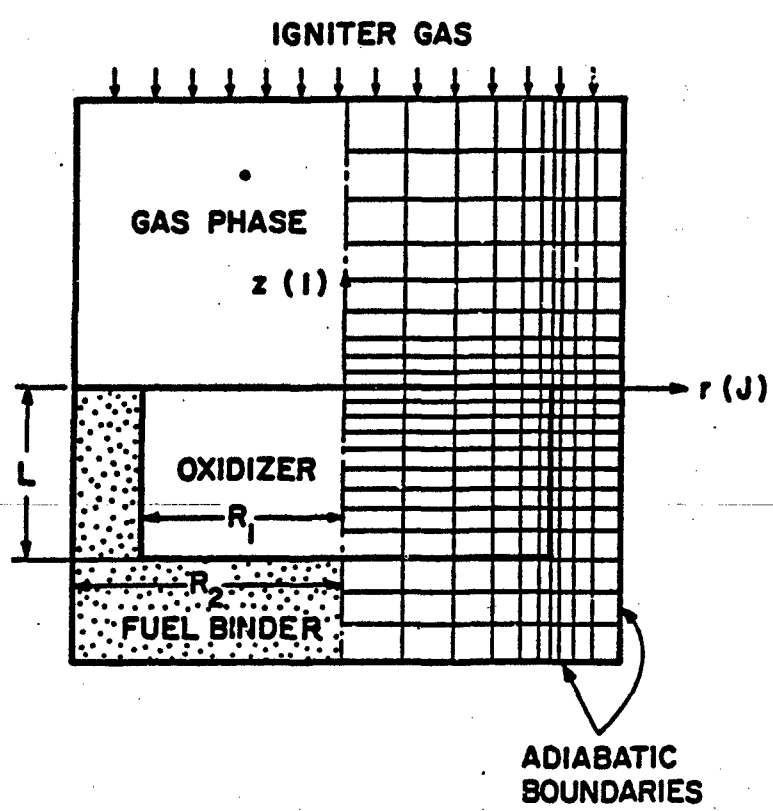
Fig. 2 Statistically Averaged Element and Finite
Difference Grid Pattern

$$\dot{q}'''_{Ox,radiation} = \tau_{Ox} G \beta_{Ox} e^{-\beta_{Ox} z} = \beta_{Ox} I_z \qquad (4)$$

and

$$\dot{q}'''_{Ox,pyrolysis} = - Z_{Ox,py} Q_{Ox,py} \exp(-E_{Ox,py}/R_u T) \qquad (5)$$

The functional form of pyrolysis heat absorption term in Eq. (5) is the same as that used by Ohlemiller and Summerfield.[15] The expression for $\dot{q}'''_{F,S}$ is similar to that of $\dot{q}'''_{Ox,s}$.

The gas-phase conservation equations are

Continuity Eq:
$$\frac{\partial \rho_g}{\partial t} + \frac{\partial (\rho_g v_z)}{\partial z} = 0 \qquad (6)$$

Energy Eq:
$$c_p \rho_g \frac{\partial T}{\partial t} + \rho_g c_p v_z \frac{\partial T}{\partial z} - \frac{\partial P}{\partial t} = \frac{\partial}{\partial z} (k_g \frac{\partial T}{\partial z})$$

$$+ \frac{1}{r} \frac{\partial}{\partial r} (k_g r \frac{\partial T}{\partial r}) + \dot{q}'''_g \qquad (7)$$

Species Eq:
$$\rho_g \frac{\partial Y_j}{\partial t} + \rho_g v_z \frac{\partial Y_j}{\partial z} = \frac{\partial}{\partial z} (\rho_g \mathcal{D} \frac{\partial Y_j}{\partial z})$$

$$+ \frac{1}{r} \frac{\partial}{\partial r} (\rho_g \mathcal{D} r \frac{\partial Y_j}{\partial r}) + \dot{\omega}'''_j \qquad (8)$$

where $j = 1, 2, 3,$ or 4 stands for the gas-phase species: oxidizer-rich gases (called Oxidizer), NO_2, IO, and fuel-rich gases (called Fuel). The symbol IO stands for intermediate oxidizer to be defined in a later section. The inhomogeneous terms $\dot{q}'''$ and $\dot{\omega}'''$ are obtained by using chemical kinetics information described in a later section.

Since the region of interest in the gas phase during the ignition process is very small (in the order of 1 mm), local pressure in this region is considered to be spatially uniform. However, the pressure is allowed to vary with respect to time. Therefore, the gas-phase momentum equations are replaced by the measured

$$P = P(t) \tag{9}$$

The equation of state for the gas phase is

$$\rho_g = \frac{P\bar{W}}{R_u T} \tag{10}$$

2.2.3 Initial and Boundary Conditions

The initial condition for the solid phase (both fuel and oxidizer) is

$$\text{at } t = 0 \quad : \quad T(0,r,z) = T_i \tag{11}$$

The boundary conditions for the solid phase are as follows. The temperature far from the interface is the same as the propellant initial temperature, i.e.

$$\text{at } z \to -\infty \quad : \quad T = T_i \tag{12}$$

Temperature continuity at various interfaces requires

$$T\Big|_{r=R_1^+} = T\Big|_{r=R_1^-} \quad \text{and} \quad T\Big|_{z=-L^-} = T\Big|_{z=-L^+} \tag{13}$$

On symmetric surfaces, adiabatic conditions are

$$\text{on } r = 0 \quad : \quad \frac{\partial T}{\partial r} = 0 \tag{14}$$

and on $r = R_2$:

$$\frac{\partial T}{\partial r} = 0 \tag{15}$$

At solid-gas and oxidizer-fuel interfaces, heat flux balance gives

$$\text{at } z = z_{s-g} \quad : \quad k_s \frac{\partial T}{\partial z}\Big|_{z_{s-g}^-} = k_g \frac{\partial T}{\partial z}\Big|_{z_{s-g}^+} + \alpha_{s-g} G +$$

$$r_{b_s} \rho_s T(c_{p_s} - c_{pg}) + \dot{q}''_{s-g} \tag{16}$$

where $\dot{q}''_{s-g}$ is the net heat generation at the surface.

at $z = -L$: $\left. k_{F,s} \frac{\partial T}{\partial z} \right|_{-L} = \left. k_{Ox,s} \frac{\partial T}{\partial z} \right|_{-L^+} +$

$$\alpha_{Ox-F} \tau_{Ox} G e^{-\beta_{Ox} L} \tag{17}$$

at $r = R_1$ and $-L < z < 0$: $\left. -k_{F,s} \frac{\partial T}{\partial r} \right|_{R_1^+} =$

$$\left. -k_{Ox,s} \frac{\partial T}{\partial r} \right|_{R_1^-} \tag{18}$$

Initial conditions for the gas-phase equations (for $j=1,2,3,4$) are:

at $t = 0$: $v_2(0,r,z) = 0$; $T(0,r,z) = T_{g,i}$; $Y_j(0,r,z) = Y_{j,i}$

$$\tag{19}$$

Boundary conditions for the gas phase are as follows. The symmetry conditions at the centerline and outer boundary give

on $r = 0$: $\frac{\partial T}{\partial r} = 0$; $\frac{\partial Y_1}{\partial r} = 0$ $\tag{20}$

and on $r = R_2$: $\frac{\partial T}{\partial r} = 0$; $\frac{\partial Y_1}{\partial r} = 0$ $\tag{21}$

Far away from the surface

$z \to \infty$: $\frac{\partial T}{\partial z} = 0$; $\frac{\partial Y_1}{\partial z} = 0$ $\tag{22}$

The temperature continuity at the interface gives

on $z = z_{s-g}$: $\left. T \right|_{z_{s-g^+}} = \left. T \right|_{z_{s-g^-}}$ $\tag{23}$

The overall and individual species mass-flux balance at the solid-gas interface is given respectively by

on $z = z_{s-g}$: $\rho_g v_z = \rho_s r_{b_s}$ $\tag{24}$

and $\rho_g v_z Y_j \Big|_{z_{s-g^-}} = \rho_g v_z Y_j \Big|_{z_{s-g^+}} - \rho_g \, \mathcal{D} \, \dfrac{\partial Y_j}{\partial z} - \dot{\omega}_j{}''$ (25)

This set of partial differential equations is being solved numerically and the solution will be presented in the future.

2.2.4 Chemical Kinetics of Nitramine Composite Propellants

It is generally known that the decomposition of nitramine dominates the overall chemical process in deflagration of nitramine composite propellants. A proper starting point in understanding the chemical kinetics of combustion of nitramine composite propellants is to investigate the pure nitramine decomposition. Due to their complexity and special characteristics, the decomposition kinetics of nitramines have been investigated extensively during the last thirty years. Recently, Schroeder[16-18], Boggs[19], and McCarty[20] have published comprehensive review articles on the kinetics of nitramine. Schroeder and Boggs studied the subject from an organic chemist's point of view while McCarty approached it from a combustion engineer's point of view. Primary $N-NO_2$ cleavage is regarded as the important initial decomposition step,[21] but there appears to be some evidence supporting two other possible initial steps in the thermal decomposition of HMX and RDX: these are unimolecular elimination reaction giving HONO and C=N double bond in the ring instead of $CH_2N_2NO_2$;[22] and unimolecular C-N bond cleavage.[23] Brill and Karpowicz[24] suggested that the initial rate controlling step for decomposition in the condensed phase involves mainly the disruption of the strong intermolecular electro-static forces between HMX molecules, and also between the HMX molecules and its decomposition products. Their postulation is based upon a comparison of Arrhenius data for phase transformation with data reported for the condensed phase decomposition process. The activation energies of the

phase transitions reflect the energy needed to disrupt electro-static forces in the crystal lattice of HMX.

Follow-up reaction steps can be divided into two categories: unimolecular and bimolecular. It appears that stepwise loss of CH_2NNO_2[23] may be an important unimolecular follow-up reaction, and that bimolecular reactions of radical or products formed in the decomposition with unreacted HMX or RDX molecules is also important. Suryanarayana et al.[23] proposed a concerted intramolecular condensed phase decomposition mechanism initiated by C-N bond fission. Gosgrove and Owen[25,26] suggested a gas phase mechanism initiated by N-N bond fission. Goshgarian[27] measured detailed concentration and temperature profiles for RDX and HMX by using mass spectrometry. The presence of NO_2 under both molten and deflagration condition was indicated, verifying the N-N cleavage is the important initial step for decomposition, and the NO_2 is a reactant of the secondary reactions in the vapor phase. Unfortunately, most investigations of decomposition kinetics of nitramines were conducted at low-temperature and low-pressure situations which may not simulate deflagration of these substances in rocket motors. Detailed mechanisms obtained by organic chemists are too complex to apply to actual highly transient ignition situations.

For kinetic mechanism in a combustion model, Ben-Reuven and Caveny[28] proposed a comprehensive kinetic model for HMX as the monopropellant, by considering a reacting molten layer coupled to the gas field through conservation conditions satisfied by all chemical species and enthalpy. The primary initial overall reaction used in Ben-Reuven and Caveny's gas-phase model of deflagration of HMX is assumed to be similar to RDX, and is represented by

$$HMX_{(g)} \longrightarrow 4/3NO_2 + 4/3N_2O + 2N_2 + 4CH_2O \tag{26}$$
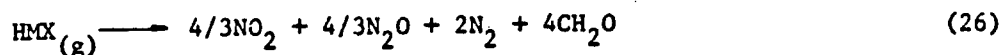
Since nitrogen dioxide reacts quite rapidly with formaldehyde, the overall consecutive reaction in the gas phase is represented by

$$7NO_2 + 5CH_2O \longrightarrow 7NO + 3CO + 2CO_2 + 5H_2O \tag{27}$$
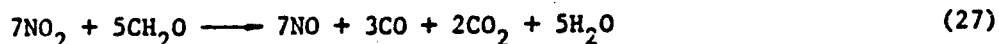
In the liquid phase, the overall reaction step was represented by

$$HMX_{(1)} \longrightarrow 4CH_2O + 3N_2O + NO + 1/2N_2 \tag{28}$$
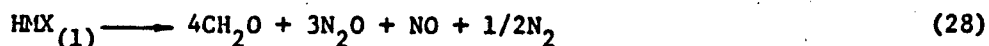
For RDX, a similar kinetic scheme was used by Ben-Reuven and Summer-field[29] and is represented by:

$$RDX_{(1)} \longrightarrow 3CH_2O + 9/4N_2O + 3/4NO + 3/8N_2 \tag{29}$$

$$RDX_{(g)} \longrightarrow NO_2 + N_2O + 3CH_2O + 3/2N_2 \tag{30}$$
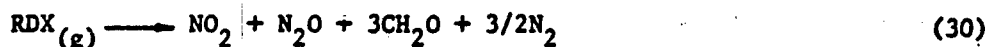
The secondary overall reaction is also the oxidization of CH_2O by NO_2 and is not repeated here.

In the ignition and combustion study of nitramine composite propellants, most attention in kinetic mechanism has been devoted to nitramine fillers; very little attention has been given to the binder. However, in order to gain deeper understanding of the ignition process and to improve the predictability of theoretical model, it is necessary to consider the role of the binder in the ignition and combustion process. Experimental results of Kubota et al.[30] revealed that flame structure, combustion mechanism, and burning rate of the HMX composite propellant are strongly influenced by the type of binders used. When a high-oxygen content binder (e.g., HTPS, HTPE,

or HTPA) was used, flame structures became homogeneous because of the form-
ation of a homogeneously mixed HMX/binder molten layer on the burning
surface. On the other hand, when a low oxygen content binder such as HTPB
was used, a large amount of carbonaceous material was formed on the burning
surface, making the structures of the burning surface and the gas phase
highly heterogeneous. The decomposition reactions of polymeric binder are
extremely complicated and are not yet fully understood. The primary decom-
position products are possibly aldehydes, hydrocarbons, and hydrogen. The
gaseous mixture of the decomposed gases of the binder is ejected into the gas
phase from the burning surface of propellant and mixed again with gases de-
composed from nitramine oxidizers. The mixture exhibits rapid exothermic
reactions which include many parallel and successive reactions.

In modeling the kinetics of nitramine composite propellant under highly
transient ignition conditions, the basic idea follows the overall reaction
representation of Ben-Reuven and Caveny in order to avoid complexity of de-
tailed kinetic mechanism. However, heterogeneous structure rather than
homogeneous molten layer is still considered valid, before onset of steady
deflagration of nitramine composite propellants. This is consistent with the
experimental test conditions which are highly transient with the enormous
heating rate at the propellant surface. A chemical reaction mechanism of the
ignition of nitramine composite propellant is proposed. It consists of the
following reactions:

(a) following the vaporization of nitramine crystals, primary gas-phase
    reaction occurs due to decomposition of HMX (or RDX) to form NO_2 and
    Intermediate Oxidizers (IO) which consists of other species than NO_2

in Eq. (26) or (30);

(b) reaction of IO species with NO_2 to form oxidizer gases (this reaction is considered to be the secondary gas-phase reaction);

(c) decomposition and pyrolysis of binder into fuel gas;

(d) oxidation of fuel gases by oxidizer gases to form final product gases; and

(e) heterogeneous reaction between oxidizer gases and solid fuel binder on the propellant surface to form final product gas.

The proposed simplified kinetic schemes and data for three types of nitramine composite propellants considered in this paper are given in Tables 1-3. The kinetic data for reaction (d) in these three tables are based upon the representative species which have the highest concentrations in oxidizer and fuel gases. In most cases, fuel gases are represented by CH_4, and oxidizer gases are represented by NO and N_2O.[31] Kinetic data of reactions (e) are largely unavailable. Representative data may be obtained in the future for major species involved in heterogeneous reactions.

2.3 Experimental Approach

2.3.1 Test Apparatus

The main test chamber with the test configuration was designed to be pressurized by high-temperature and high-pressure gases generated in a solid-propellant driving motor. Pressurization rates of the test chamber closely simulate conditions during the ignition transient of actual rocket motors.

Table 1. Kinetic Scheme and Data for Ignition of
HMX/CTPB Composite Propellants

Kinetic Data / Reaction	Pre-exponential Factor	Activation Energy	Heat of Reaction	Source
(a) $HMX \rightarrow NO_2 + 7.67$ IO	$1 \times 10^{16.4}$ 1/s	1.931×10^8 J/kmole	-5.166×10^8 J/kmole	Ben-Reuven Caveny (1979)
(b) $NO_2 + 7.67$ IO $\rightarrow 9.62$ OX	1×10^6 m^3/kmole-s	0.802×10^8 J/kmole	-1.923×10^8 J/kmole	Ben-Reuven Caveny (1979)
(c) $CTPB \rightarrow F$	128 kg/m^2-s	0.4389×10^8 J/kmole	1.59×10^6 J/kg	Cohen Fleming Derr (1974)
(d) 4.361 OX + F $\rightarrow 8.668$ P	1×10^{16} m^3/kmole-s	0.4×10^8 J/kmole	-7.4×10^7 J/kmole	Drummond* (1969)
(e) OX + CTPB $\rightarrow 1.99$ P	----	----	----	----

*Kinetic data are based on the representative species which have the highest
concentration in oxidizer and fuel gases.

Table 2. Kinetic Scheme and Data for Ignition of
RDX/CTPB Composite Propellants

Reaction / Kinetic Data	Pre-exponential Factor	Activation Energy	Heat of Reaction	Source
(a) $RDX \rightarrow NO_2 + 5.5\ IO$	$1 \times 10^{15.5}$ 1/s	1.73×10^8 J/kmole	-3.97×10^8 J/kmole	Ben-Reuven Caveny Summerfield Vichnevetsky (1976)
(b) $NO_2 + 5.5\ IO \rightarrow 6.14\ OX$	1×10^9 m^3/kmole-s	0.79×10^8 J/kmole	-1.923×10^8 J/kmole	Ben-Reuven Caveny Vichnevetsky Summerfield (1976)
(c) $CTPB \rightarrow F$	128 kg/m^2-s	0.4389×10^8 J/kmole	1.59×10^6 J/kg	Cohen Fleming Derr (1974)
(d) $3.71\ OX + F \rightarrow 8.668\ P$	0.95×10^{16} m^3/kmole-s	0.4×10^8 J/kmole	-7.2×10^7 J/kmole	Drummond* (1969)
(e) $OX + CTPB \rightarrow 2.34\ P$	----	----	----	----

*Kinetic data are based on the representative species which have the
highest concentration in oxidizer and fuel gases.

Table 3. Kinetic Scheme and Data for Ignition of
HMX/HTPB Composite Propellants

Reaction / Kinetic Data	Pre-exponential Factor	Activation Energy	Heat of Reaction	Source
(a) $HMX \rightarrow NO_2 + 7.67$ IO	$1 \times 10^{16.4}$ 1/s	1.931×10^8 J/kmole	-5.166×10^8 J/kmole	Ben-Reuven Caveny (1979)
(b) $NO_2 + 7.67$ IO $\rightarrow 9.62$ OX	1×10^6 m^3/kmole-s	0.802×10^8 J/kmole	-1.923×10^8 J/kmole	Ben-Reuven Caveny (1979)
(c) $HTPB \rightarrow F$	2990 kg/m^2-s	0.7064×10^8 J/kmole	1.81×10^6 J/kg	Cohen Fleming Derr (1974)
(d) 4.290 OX $+ F \rightarrow 8.53$ P	0.9×10^{16} m^3/kmole-s	0.39×10^8 J/kmole	-7.3×10^7 J/kmole	Drummond* (1969)
(e) OX $+ HTPB \rightarrow 1.99$ P	-----	-----	-----	----

*Kinetic data are based on t'e representative species which have the highest concentration in oxidizer and fuel gases.

High pressurization rates obtained in this setup can also simulate those conditions encountered during onset of DDT. Using this test rig, it is possible to obtain pressures up to 50 MPa (~ 7000 psi), and pressurization rates up to 150 GPa/s ($\sim 1.5 \times 10^6$ atm/s).

A schematic diagram of the test section is shown in Fig. 3. A crack-like cavity, formed between a transite slab and a plexiglass window, is situated normal to the flow direction of gases in the main chamber. The gap width of the crack is determined by the recessed depth of the transite slab in the test configuration. Because the main motivation of this work is to study the effect of propellant ingredients, the gap width was held constant, and equal to 1.27 mm. The cavity length for the test configuration was 161 mm. As shown in Fig. 3, two propellant test samples are located at the tip of the cavity. Two pressure transducer ports are provided in the crack cavity: one near the test sample shown in Fig. 3, and the other at the crack entrance. The ignition event is observed through a set of transparent plexiglass windows. The window assembly is held in place by a window retainer, which forms the front half of the chamber shown in Fig. 4. With the exception of the exit nozzle through which gases are discharged into the atmosphere, the chamber is completely sealed during tests. For safe operation, the chamber is also equipped with a safety head, which houses a bursting diaphragm; the diaphragm ruptures at a prespecified pressure of 70 MPa ($\sim 10,000$ psi). The driving motor system used in this study is a small solid-propellant motor initiated by an electric primer. Details of the driving motor system can be found in Ref. 32. The high-temperature combustion product gases generated in this motor flow through a multiperforated nozzle into the main test chamber, and pressurize the chamber at high loading rate.
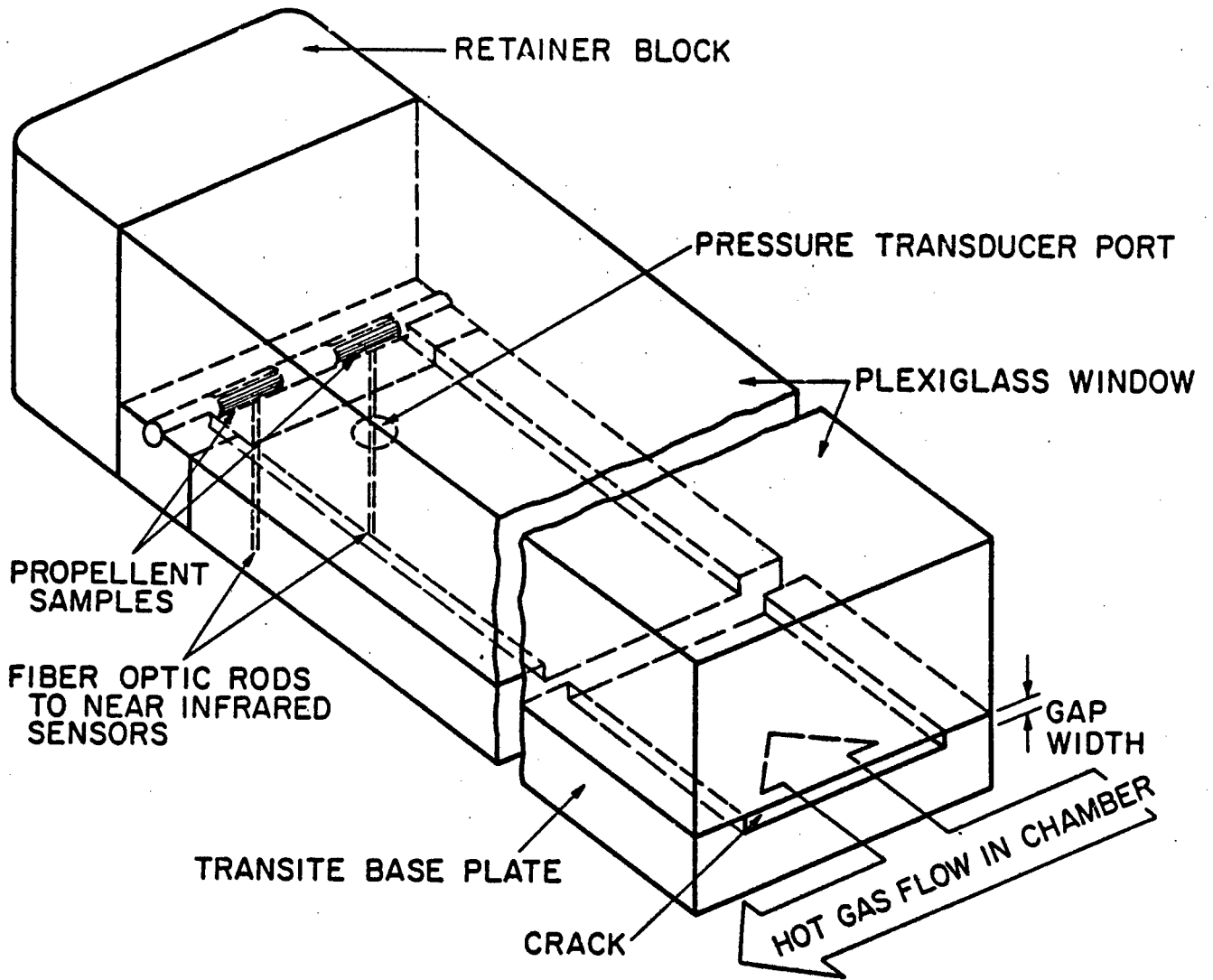
Fig. 3   Schematic Diagram of the Test
Section for Ignition Experiments
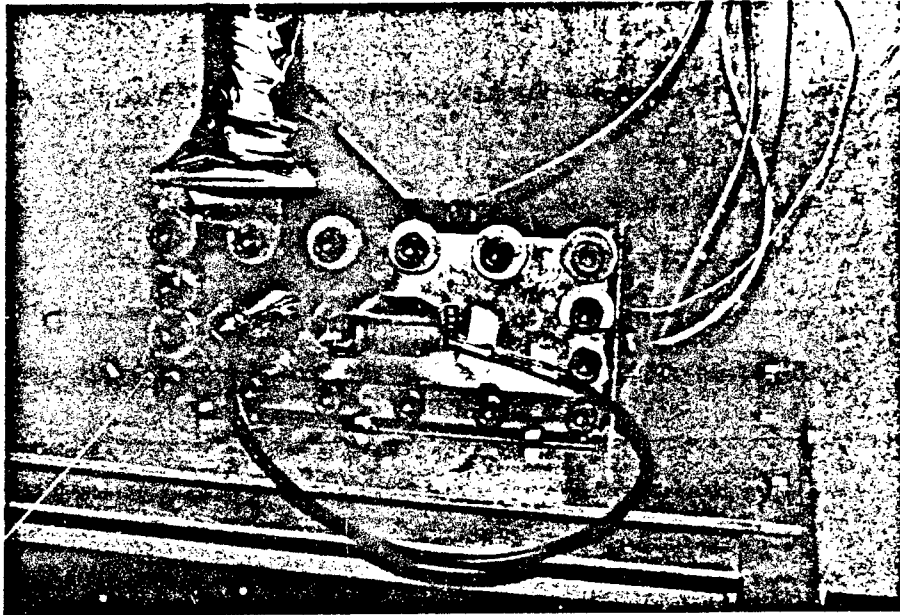
Fig. 4 Photograph of the Assembled Test Rig

Figure 4 shows the assembled test chamber. The driving motor is located immediately below the base mounting plate, and hence cannot be seen in this photograph. Exhaust gases from the driving motor flow vertically upward into the main flow channel located at the left end of the test chamber. The test chamber has two window openings. In order to have a close-up view of the ignition process near the right most portion of the longer window, a light pipe and a prism were used to give light signals at the onset of the hot gas flow in the test chamber. By so doing, the event of onset of hot gases (signified by a bright circular spot) and the ignition process can be photographed simultaneously on the high-speed film. Before most test firings, a nitrogen feedline is turned on to purge the chamber, eliminating oxygen in the test chamber during initial ignition. Purged gases leave the test chamber through the exhaust pipe mounted vertically on the left side of the test chamber. The purpose of driving oxygen from the system is to reduce the complexity of the ignition process so that oxygen will not participate in the ignition and combustion processes.

Special features of the test configuration are near-infrared photodiodes used to sense infrared radiation from surfaces of propellant samples, and the sample holder configuration is designed to provide a clear view of the ignition event. The near-infrared photodiode is the product of Texas Instruments Company (T. I. No. 1N2175), with photocurrent rise time about 2 μs and spectral response range from 0.42 μm to 1.12 μm. As shown in Fig. 5, two near-infrared photodiodes are installed into the chamber. Infrared light emitted from the burning surface of the propellant sample passes through a fiber optic rod and a glass rod window, and is sensed by the near-infrared photodiode. To measure the sensitivity of the near-infrared photodiode in

PROPELLENT SAMPLES   SAMPLE HOLDER
A AND B

TRANSITE BASE PLATE

FIBER OPTIC ROD

FIBER OPTIC ROD HOLDER

GLASS ROD WINDOW

PHOTODIODE HOLDER

NEAR INFRARED PHOTODIODE
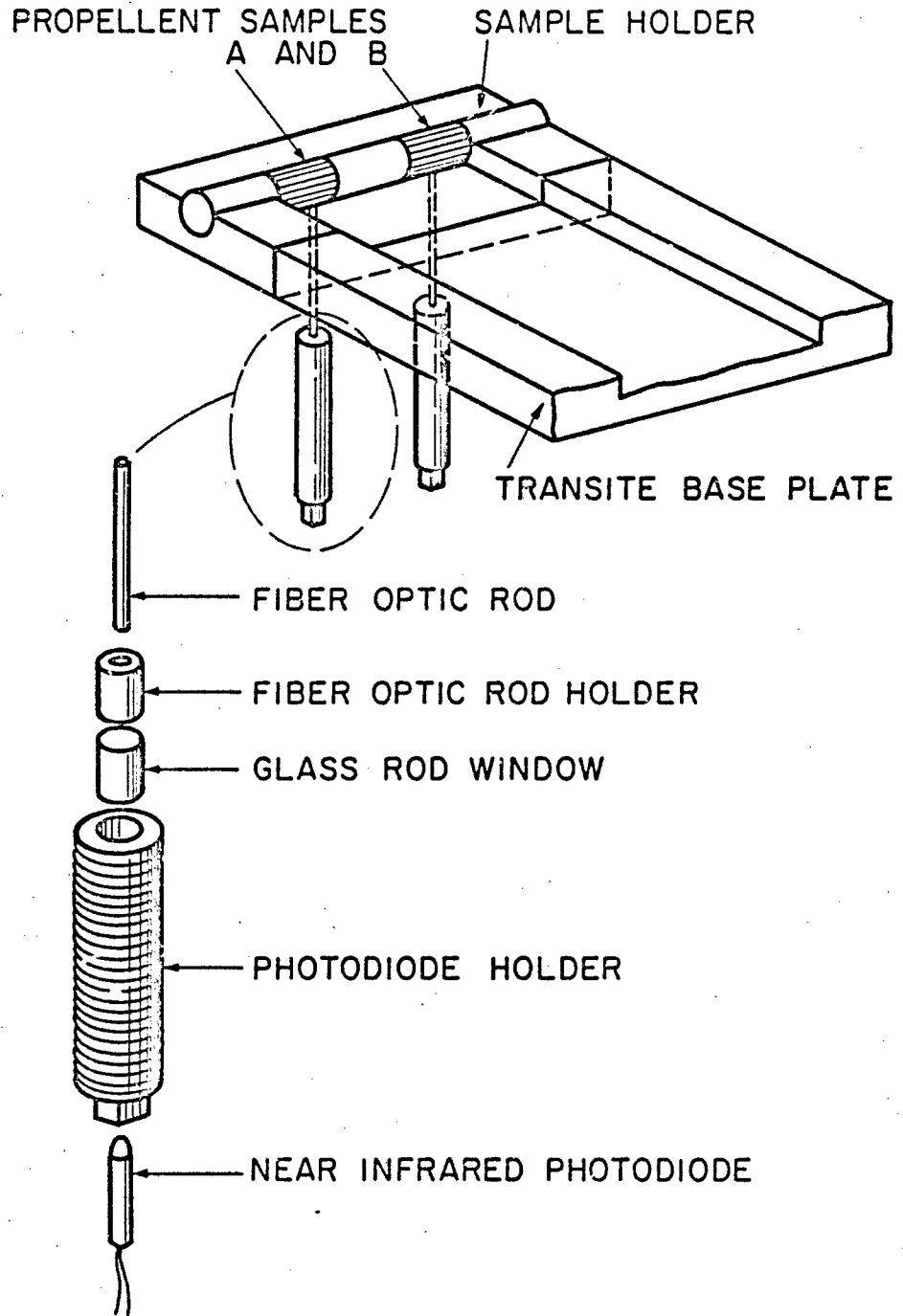
Fig. 5 Detailed Schematic Diagram of
the Setup in Test Configuration B

response to gas-phase radiation from propellant flames, separate tests were conducted. It was found that the gas-phase radiation cannot be detected by the near-infrared photodiode; only the near-infrared light from the burning solid surface can be monitored. This implies that the signal recorded by the sensor represents the surface temperature rise rather than the arrival of hot gases. Based upon the distinct feature of the near-infrared sensor, this test configuration was used in most of the test firings. An external photodiode system, consisting of photographic lens mounted on an optical bed, a fast-response photodiode, and an amplifier, was also used in the test configuration.

The data acquisition system used in the present study is very similar to that described in the paper by Siefert and Kuo.[32] This system is comprised of (1) pressure measuring system, (2) near-infrared photodiode (or ionization pin) setup, (3) high-speed photography system, (4) photodiode system, and (5) transient waveform recording system. Piezoelectric quartz transducers with a rise time of 1.5 μs and natural frequency of 300 kHz were used to measure the pressure. The near-infrared photodiode system, photodiode system, and a 16 mm Hycam movie camera were used in most of the tests, and the time interval between consecutive pictures is about 60 μs. At ignition, it is expected that the near-infrared photodiode signal will begin to rise abruptly, and that a bright light will appear at the propellant surface on the film. Therefore, to determine the onset of ignition, the following procedure, in which the film is read in conjunction with the photodiode system, is adopted:

(1) the picture that shows the first occurrence of bright light is defined as t_{film},

(2) the corresponding point is located on the photodiode signal, and

(3) the point of abrupt rise in the photodiode signal within 30 μs of t_{film} is taken as the actual time for onset of ignition.

2.3.2 Propellants Used in Experiments

Three types of nitramine propellants (1, 2, and 3) were used in experimental study. Propellant 1 is HMX-based composite propellant with 79% HMX and 21% CTPB binder mix. Propellant 2 is RDX-based composite propellant with 79% RDX and 21% CTPB binder mix. The comparison of propellant 1 and 2 gives the effect of nitramine filler. Propellant 3 is HMX-based composite propellant with 80% HMX and 20% HTPB binder mix. The binder effect can also be studied by comparing the results of propellant 1 and 3. Several important thermal properties of propellants and their products are tabulated in Table 4. Some of the physical properties of HMX, RDX, HTPB, and CTPB are tabulated in Table 5.

2.4 Results and Discussion

Figure 6 shows a typical set of time correlated data which includes trigger pulse (common time signal), pressure at the crack entrance (G2), pressure at the crack tip (G3), near-infrared photodiode signals (NI1 and NI2) for propellant samples HMX/CTPB and HMX/HTPB, and photodiode signal in the region near HMX/CTPB sample. Trigger pulse is generated by a light-emitting diode (LED) driver unit, and is used to correlate time between data obtained from high-speed movie films and transient waveform recording devices. When hot gases from the driving motor reach the crack entrance, pressure at the entrance increases rapidly. The first discernible pressure

Table 4. Thermal Properties of Three Types of Nitramine
Composite Propellants and Their Products

Properties / Propellant Types	(1) $\frac{HMX}{CTPB}$	(2) $\frac{RDX}{CTPB}$	(3) $\frac{HMX}{HTPB}$
Density (kg/m^3)	1,650	1,570	1,580
Thermal Diffusivity (m^2/s)	0.1152×10^{-6}	0.096×10^{-6}	0.11×10^{-6}
Flame Temperature (K)	2,379	2,387	2,363
Ratio of Specific Heat, γ	1.27	1.27	1.27
Av. Mol. Wt. of Product Gases (kg/kmole)	19.59	19.58	19.33

Table 5. Properties of Nitramine Propellant Fillers and Binders

Properties \ Ingredients	HMX	RDX	HTPB	CTPB
c (J/kg-K)	1797.0	1864.0	1814.0	1768.0
k (W/m-K)	0.3762	0.2918	0.1840	0.2236
ρ (kg/m^3)	1910.0	1820.0	920.0	930.0
α (m^2/s)	0.11×10^{-6}	0.086×10^{-6}	0.11×10^{-6}	0.136×10^{-6}

rise at the tip occurs some time later than the corresponding pressure rise at the crack entrance. The rising portion of the pressure trace at the crack tip is quite linear, and the averaged pressurization rate at the tip can be obtained easily. In order to measure the time required for the onset of gas evolution, the first discernible pressure rise at the tip is chosen as the time equal to zero. Shortly after the pressure rise at the tip, the near-infrared photodiode signals for the propellant samples show abrupt rises, especially for NI1. These rises correspond to the increase of the surface temperatures of propellant samples. After analyzing the motion picture films, the onsets of gas evolution of two propellant samples are marked as two black dots on the near-infrared photodiode signals. As shown in Fig. 6, the onset of gas evolution occurs during the uprising portion of the near-infrared photodiode signal, rather than the peak of the near-infrared photo-diode signal. The external photodiode signal (PD) for detecting light intensity near the HMX/CTPB propellant sample also shows a similar rise with NI1.

The consistency between the two independent measuring systems is helpful in determining the time of onset of gas evolution. In this particular case, the HMX/CTPB propellant begins to gasify slightly sooner than the HMX/HTPB propellant. After momentary ignition, both propellant samples were extinguished; thus the two black dots in Fig. 6 can be regarded only as onset of gas evolution, and not as onset of ignition. After the strong pulse, near-infrared photodiode signals decrease, due to the extinguishing of propellant samples, and in part to the coating on the end of the fiber optic by product gases from the driving motor and pyrolyzed gases from propellant samples.
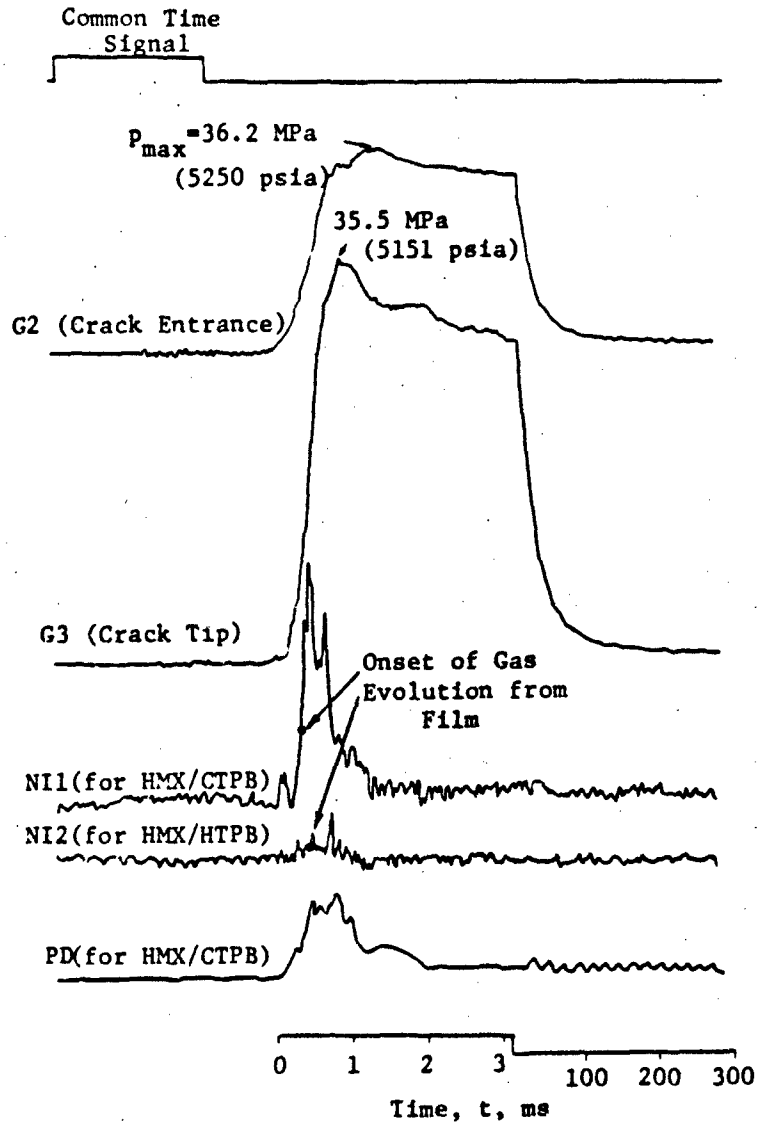
Fig. 6 A Typical Set of Time Correlated Data of a
Test Firing with Two Different HMX-Based
Composite Propellants

Figure 7 shows the experimental data of onset of gas evolution of two HMX-based propellant samples as a function of the pressurization rate. These two propellants have nearly the same weight percentage of HMX, but with different binder mixes (CTPB and HTPB). Although a few tests using these two propellants under identical operating conditions suggest that the time required for onset of gas evolution is slightly shorter for HMX/CTPB propellant, there is no absolute indication that this is true for all circumstances.

Data shown in Fig. 7 were compiled from a number of test firings, and could be considered more or less one family and fitted by a single curve. One possible reason for this is that the low percentage of weight fraction of binder (~ 20%) does not make the binder effect very pronounced. It is quite obvious that the time required for onset of gas evolution decreases with the increase of pressurization rate. It should be noted that none of these data corresponds to sustained ignition; hence the curve can only be regarded as the boundary of onset of gas evolution. One major reason for the fact that the tests did not sustain ignition is the short action time of the solid propellant driving motor (less than 50 ms).

The weak effect of binder may be explained by the following consideration. As it is noted above that in several test firings conducted with HMX/CTPB and HMX/HTPB as samples in the same test firing, under the same operating situation, the time required for onset of gas evolution of HMX/HTPB was slightly longer than that of HMX/CTPB. Table 5 shows that the thermal diffusivity of CTPB is larger than that of HTPB, which implies that under the same heating condition the surface temperature of HTPB will rise faster than
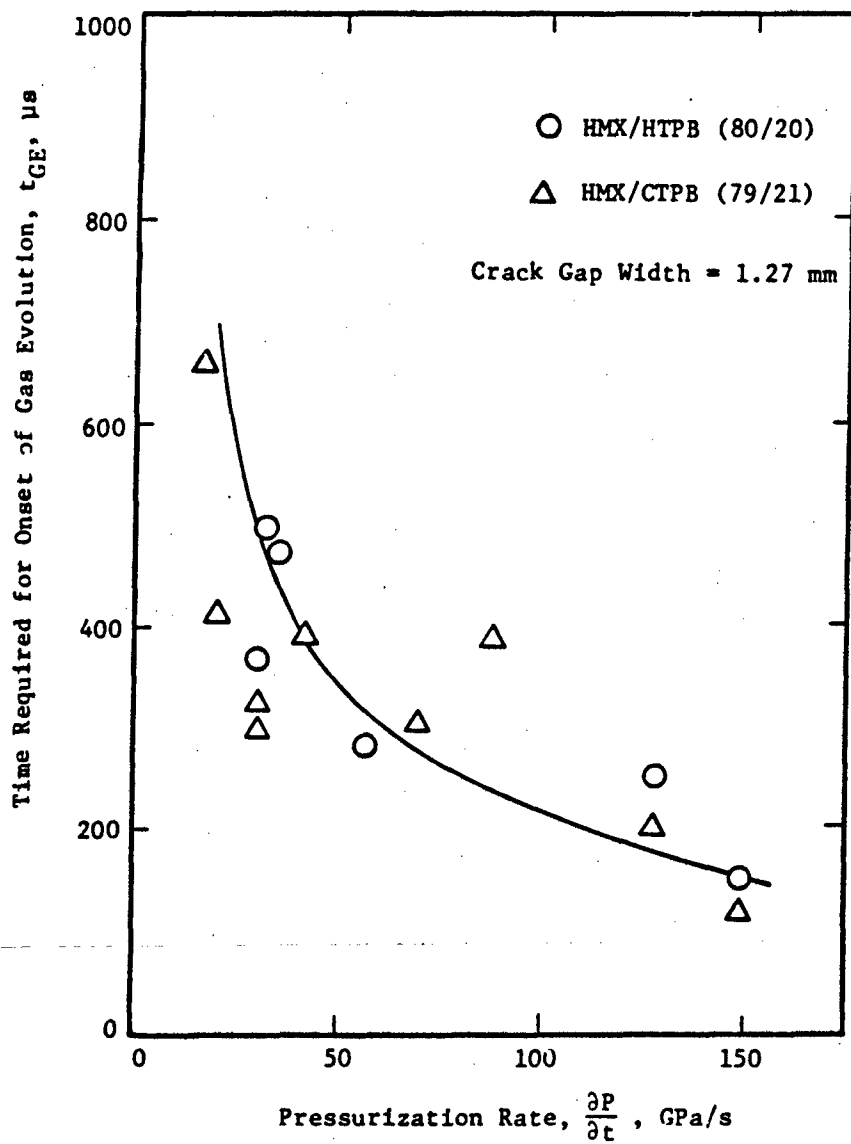
Fig. 7   Onset of Gas Evolution Time as a Function of
Pressurization Rate for Two HMX-based Composite
Propellants

that of CTPB. However, using Table 1 and 3, it can be seen that the activation energy of the pyrolysis of CTPB is less than that of HTPB, which implies that the energy barrier of pyrolysis of CTPB is lower than that of HTPB. Although the thermal diffusivity effect and activation energy effect work in opposite directions, the experimental data show that the onset gas evolution of HMX/CTPB is earlier than that of HMX/HTPB. Thus, it is reasonable to conclude that activation energy of pyrolysis of the binder is more important than the thermal diffusivity effect.

Figure 8 shows the comparison of the times required for gas evolution of RDX/CTPB propellant (dashed line) and HMX-based composite propellants (shown as solid line transferred from Fig. 7). On the same figure, the ignition delay of AP-based composite propellant is also plotted. In this figure, all data of AP-based composite propellants correspond to sustained burning after ignition, while only one datum of RDX/CTPB (marked by *) at the lowest dp/dt corresponds to sustained burning. It is well known, that the difference between the time required for gas evolution and ignition is a function of heating rate. This difference is very pronounced for nitramine propellants. The time difference becomes smaller at low heating rates (or dp/dt). Thus, it is not surprising to obtain sustained burning of RDX/CTPB at low dp/dt. It is shown in this comparison that the ease of ignitability increases in the following order: HMX-based, RDX-based, and AP-based composite propellants. From Tables 1 and 2, one can see that the activation energy of decomposition of RDX is lower than that of HMX. Also, Table 4 shows that the thermal diffusivity of RDX/CTPB propellant is lower than that of HMX/CTPB. Therefore, RDX/CTPB is easier to reach onset of gas evolution than HMX/CTPB. Obvious divergences of three boundary curves of HMX-based, RDX-based, and AP-based
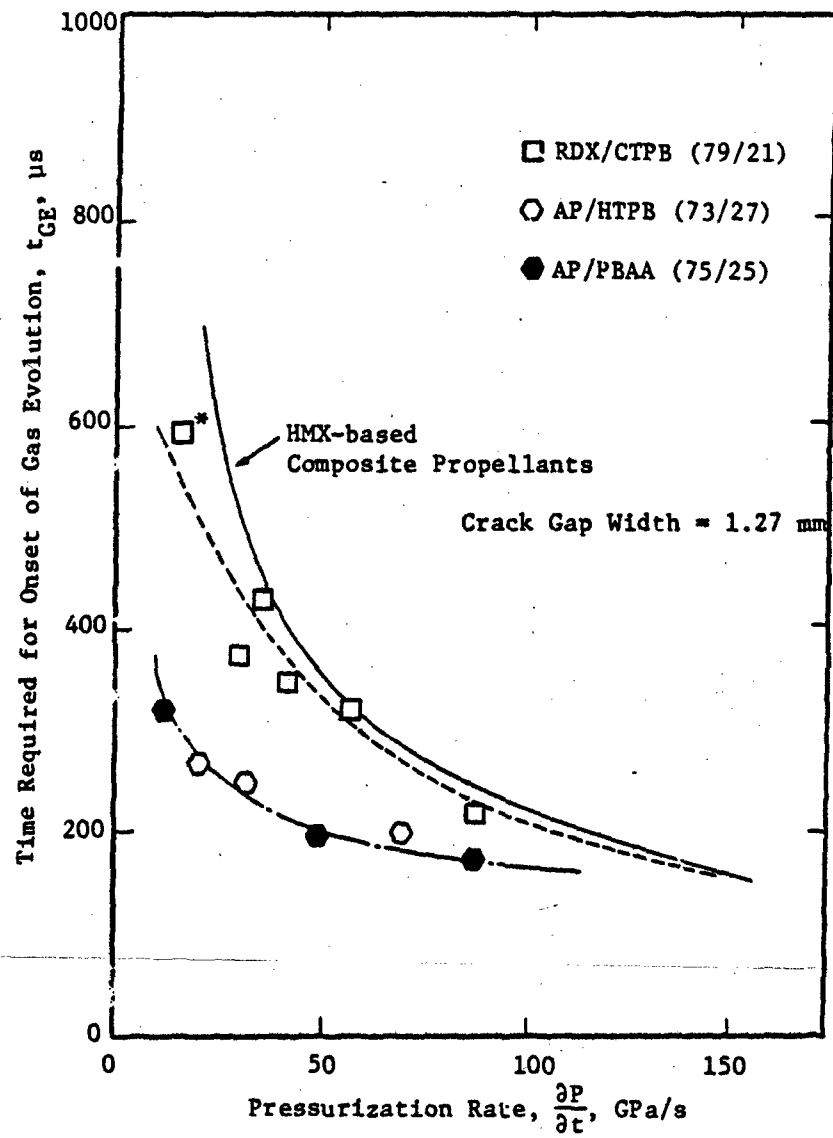
Fig. 8 Comparison of the Dependence of Onset of Gas
Evolution on Pressurization Rate for Various
Types of Composite Propellants

composite propellants can be observed at low dp/dt, while these divergences tend to diminish at high dp/dt. The observed convergence of these boundaries at high pressurization rates is mostly due to the high heating rates which effectively reduce the influence of both thermal diffusivity and chemical kinetics.

Figure 9 shows a series of photographs developed from a high-speed movie film obtained in a test firing using the test configuration. This photograph sequence is helpful in illustrating the ignition event. The crack tip is located on the right hand side of the photograph. Hot gases generated in driving motor travel from left to right. At the lower left corner of each photograph, there is a prism which shows the onset of light through a light pipe (see Fig. 4) upon the arrival of the hot gases at the crack entrance. In this test firing, RDX/CTPB propellant sample is installed at the lower portion and HMX/CTPB propellant sample is located at the upper portion. The crack tip region is pressurized at a rate of 16 GPa/s. The time period between consecutive pictures is about 65.6 µs. Picture No. 1 shows a dim dot of light on the prism indicating the arrival of hot gases at the crack entrance. After the reflection of the compression wave at the crack tip, a bright region due to further reactions of hot gases is initiated at the crack tip (Picture No. 2). The reaction front then propagates to the left at a velocity of 88 m/s relative to the stationary coordinate. This reaction front propagation causes the expansion of the bright gas region in Pictures 3-8. As time goes on, the luminous zone is reduced; this is probably due to the continuous chamber pressurization by product gases from the driving motor. The incoming gases driven by the stronger pressure gradient, compress the gas-phase reaction region and reduce the size of the luminous zone. The re-
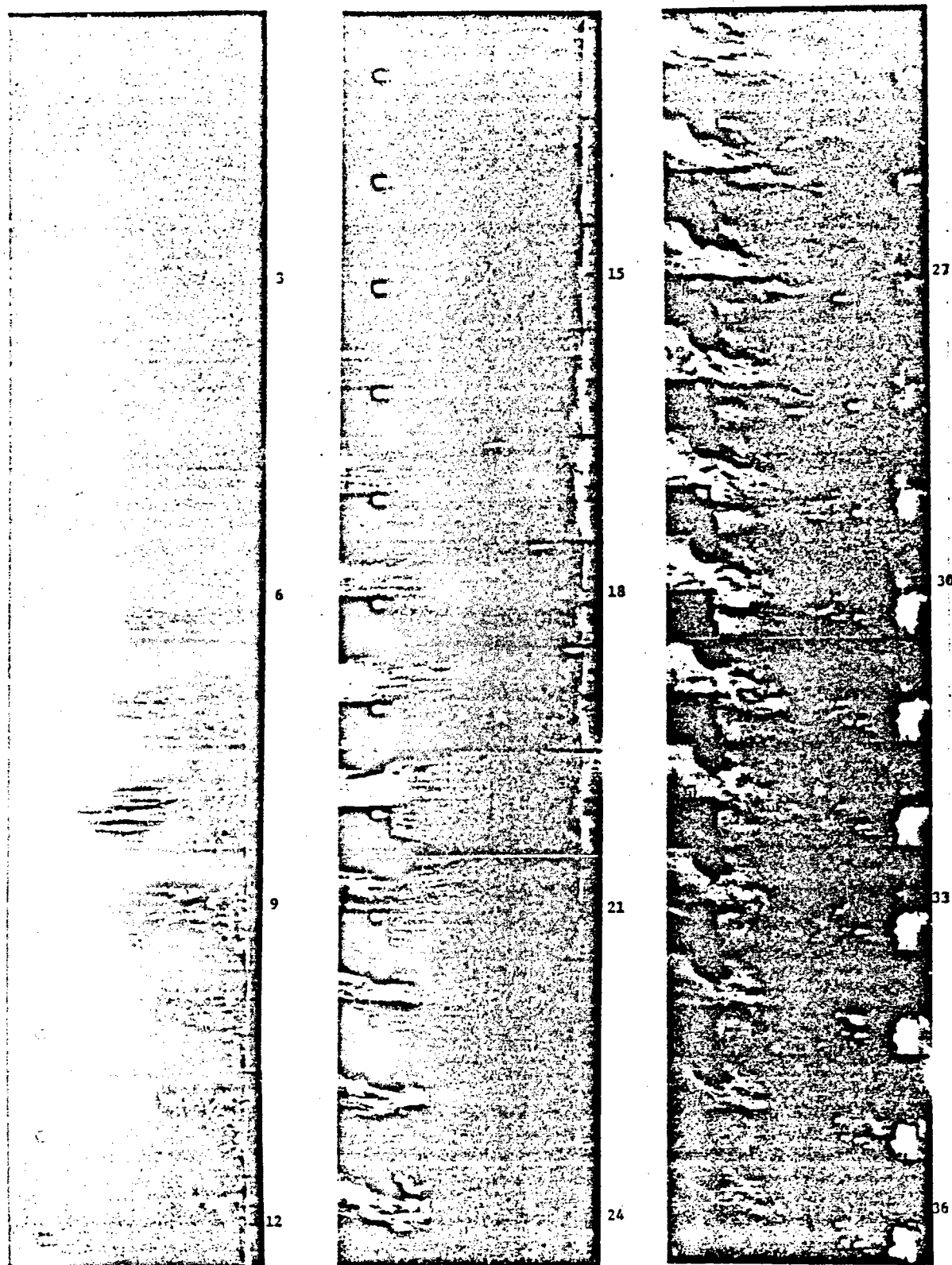
Fig. 9 High Speed Photographs of Ignition Process of Nitramine Composite
        Propellants

duction of luminous zone is also partly caused by the local pressure increase which shortens the reaction time. These phenomena are shown in Pictures 8-15. In Picture 11, the surface of RDX/CTPB propellant sample starts to show some brightness, which indicates the onset of gas evolution of RDX/CTPB propellant, while the surface of HMX/CTPB propellant is still dark. [It should be noted that Pictures 8, 9, and 10 also have some bright lines near the crack tip; however, these bright lines are due to the reflection of light from metal surfaces of the sample holder.] Picture 12 shows that HMX/CTPB sample begins to gasify. The HMX/CTPB sample remains ignited until Picture 23 and then extinguishs thereafter. The RDX/CTPB sample is nearly extinguished as shown in Picture 23 and it becomes definitely ignited again as shown in Picture 24. This ignition was sustained throughout the test firing. In the later phase, more bright gases from the driving motor enter the crack cavity. Due to the increase in luminosity, and slight gas penetration between the plexiglass window and protruded surfaces of the transite base plate, the screw heads on both sides of the channel become visible as black circles. It is interesting to note that the last ten pictures in Fig. 9 showed some burning particles above the RDX/CTPB surface. These particles could either come from the burning propellant sample due to ejection of micro-mechanical fractured pieces or from the driving motor system. At the present time, the source has not been fully identified, and this phenomenon is subjected for further investigation.

The momentary-ignition (gas evolution processes followed by extinction) phenomenon of HMX/CTPB propellant can be explained as follows. When heating rate is very high, a thin thermal layer near the propellant surface is generated. If the burning rate of this hot thin layer of the propellant is higher

than the rate of thermal wave penetration, as this hot layer burns out, a new thermal layer may not have a chance to be established for sustained burning. Thus, propellant sample is extinguished after the first thermal layer is burned out. The chemical kinetic characteristics for solid propellants also have significant influence on the momentary ignition phenomenon. Since RDX/CTPB propellant requires lower activation energy than HMX/CTPB, it is easier to establish self-sustained ignition as shown in Pictures 24 onwards.

III. MECHANISM OF CRACK PROPAGATION IN BURNING SOLID PROPELLANT

3.1 Motivation and Objectives

Increase in burning surface area caused by propagating cracks can affect the actual performance of a rocket motor and in the extreme could lead to deflagration-to-detonation transition (DDT) or transition to detonation due to some unresolved mechanisms (XDT). The study of propagating cracks in solid propellants under closely simulated motor operating conditions is therefore important in understanding the off design operation and detonation initiation phenomena in solid propellants.

One of the major objectives of this research program is to gain deeper understanding of the mechanism of solid propellant grain fracture during rocket motor firing. This subject is of special interest to investigators of rocket motor grain integrity. Numerous studies have been conducted to investigate crack propagation phenomena by employing only solid-mechanics analyses and experimental procedures. However, very little effort has been made on crack propagation of solid propellants under burning conditions. It is, therefore, quite obvious that the study of crack propagation in burning solid propellants would be most realistic and instrumental in understanding the mechanism of grain fracture due to crack propagation under rocket motor operating conditions.

Specific objectives of this investigation were:

1. To develop an experimental technique to study crack propagation in a composite propellant under burning conditions;

2. to determine crack propagation velocities in solid propellant samples under burning conditions;

3. to observe any abnormalities of the propagating crack;

4. to study the effects of chamber pressure, pressurization rate, and crack sample geometry on crack propagation velocity;

5. to analyze the stress and strain state at the crack tip by utilizing a finite element analysis;

6. to compare the observed mass burning rate with that calculated from steady-state burning rate law;

7. to modify the existing test rig so that the burning can be interrupted and the sample can be recovered; and

8. to postulate and identify the major mechanism of dynamic crack propagation.

3.2 Setup of Crack Propagation Test Rigs

Two windowed test chambers, one small and one large, have been designed and constructed for observing the crack propagation phenomena in burning solid propellant samples. The small test rig was adapted from the chamber used for tip ignition studies. The schematic diagram and a part of the results obtained from this chamber were included in the last annual report. In order to study the crack propagation phenomena under more suitable conditions, a number of modifications were incorporated into the design of a

larger test rig. A schematic diagram of this test rig is shown in Fig. 10.

Specific features and improvements of the second test rig are:

a)   increased chamber width;

b)   increased chamber depth;

c)   stronger window retainer design;

d)   more complete instrumentation and data acquisition; and

e)   improved safety characteristics.

With the increased chamber width, the sample geometry becomes more flexible and the influence of reflected compression waves from chamber walls is significantly reduced. Also, the crack propagation time period is made long enough to allow more detailed observations of the physical process. By increasing the chamber depth, possible leaks between the driving motor assembly and the main chamber are eliminated. In addition, thicker plexiglass windows can be used to strengthen the window assembly so that the possibility of flame spreading between the propellant sample and sacrificial window is substantially reduced.

A photograph of the main chamber and window retainer is shown in Fig. 11.   The window assembly consisting of a 1/2" thick sacrificial window and a 3" thick main window are shown together with the window retainer in Fig. 12.

In the large test chamber, two window openings (a circular and a rectangular one) were made in the window retainer. The purpose of designing two
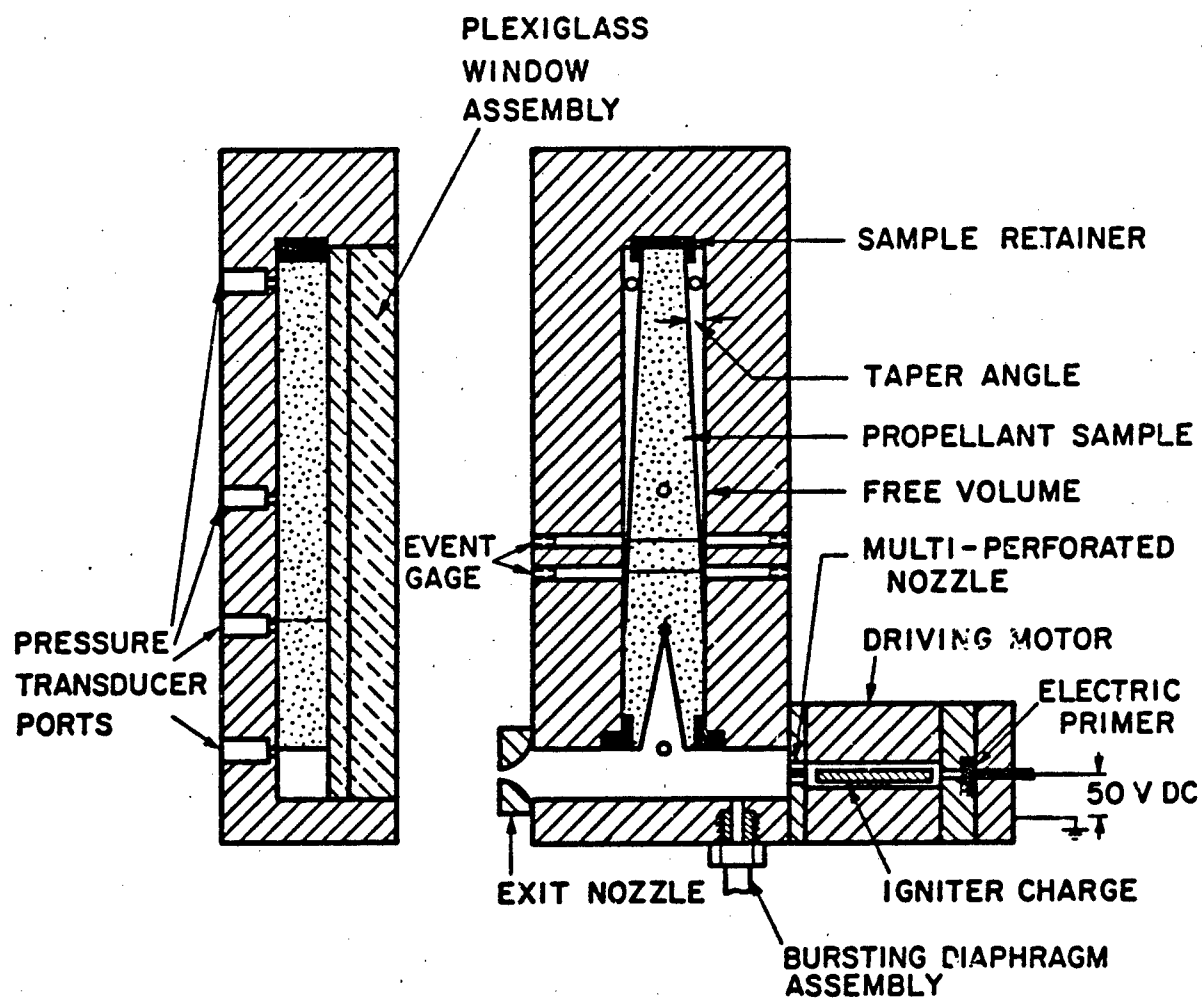
Fig. 10 Schematic Diagram of Crack Propagation Chamber
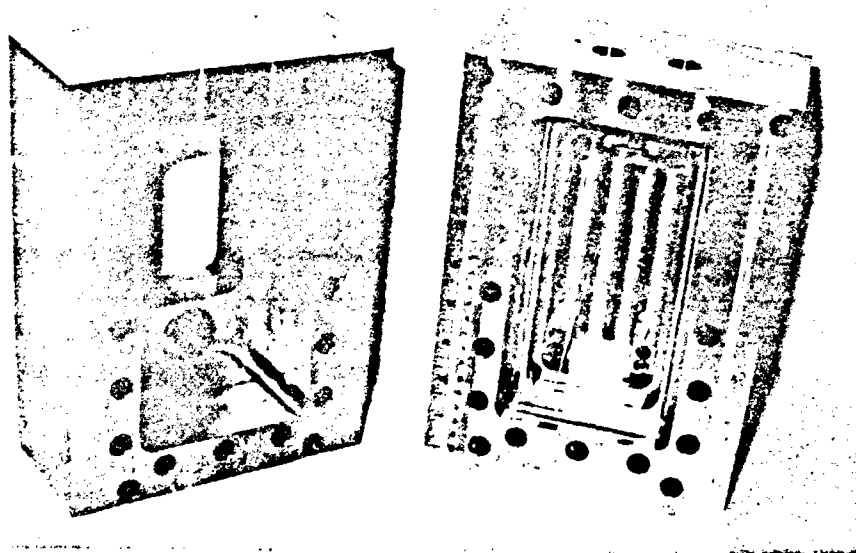
Fig. 11 Photograph of the Main Chamber and Its Window Retainer
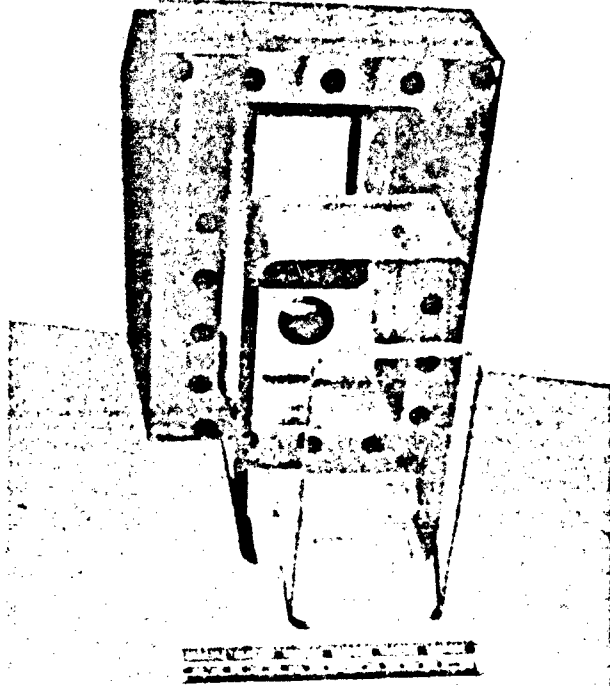
Fig. 12 Photograph of Window Assembly and Retainer

viewing openings instead of a single long one is to avoid window buckling and retainer plate warpage. Through the circular opening, one could observe the onset of the combustion product gases entering the test chamber from the driving motor.

In the large test rig, more pressure transducers were used for recording p-t traces during test firings. A maximum of six piezoelectric transducers can be used simultaneously. One of these transducers could be mounted on the driving motor and the rest mounted on the main chamber at the crack entrance, initial crack tip region, the center of the sample beyond the initial crack tip, the upper cavity, and the lower cavity (see Fig. 10).

Two ports for mounting break wires or thermocouples in the main chamber were designed and constructed to detect the arrival of the hot gases penetrating the propellant sample at the crack tip. Ports were made in the free volume regions of the chamber for optical illumination of the sample surfaces which are not initially in contact with the combustion gases. This is useful for obtaining information of the instantaneous boundaries of the propellant sample in the free volume region. These two illumination ports can also be used for other purposes as well; for example, one could mount transducers, photodiodes, break wires, or thermocouples so that measurements can be made in the free volume regions or the upper part of the propellant sample. An additional port for collecting combustion product gas samples was also machined in the main chamber to obtain species concentration at a specified time period during crack propagation.

An assembly of safety head, consisting of a specified bursting pressure diaphragm and a retainer is installed near the entrance of the main test

chamber (see Fig. 10). This setup keeps the chamber safe in case of over-pressurization. It is also advantageous for obtaining higher rates of de-pressurization, since this can help the recovery of the propellant sample by quenching the burning surfaces.

In sample preparation, a propellant block is first machined to the desired dimensions. It is then clamped in between two plexiglass tamplets for trimming into a final configuration (see Fig. 13). A 3-mm deep slit is made by a sharp razor blade at the crack tip to help the initiation of the crack growth under rapid pressurization.

It is important to note that shortly after the flame has reached the tip of the narrow slit, the subsequent crack propagation beyond the original tip of the slit will have natural crack geometry rather than the artificial geo-metry of the initial slit. Also, the triangular opening of the propellant sample at the entrance is to facilitate pressure loading on the slanted sur-faces. The wide triangular opening should not be regarded as a part of the initial crack tip contour. The essential part of crack geometry is the pre-fabricated slit. The type of the propellant used was AP/HTPB (73/27) with an average AP particle size of 200 m.

Figure 14 shows a closeup view of the propellant installed in the test chamber. The sample is held in its position by three brass retainers. The plexiglass window assembly is designed to compress the sample between the rear wall of the chamber and the window to avoid any leakage.

A photograph of the assembled test rig is shown in Fig. 15. In this setup the driving motor is mounted below the horizontal metal plate and
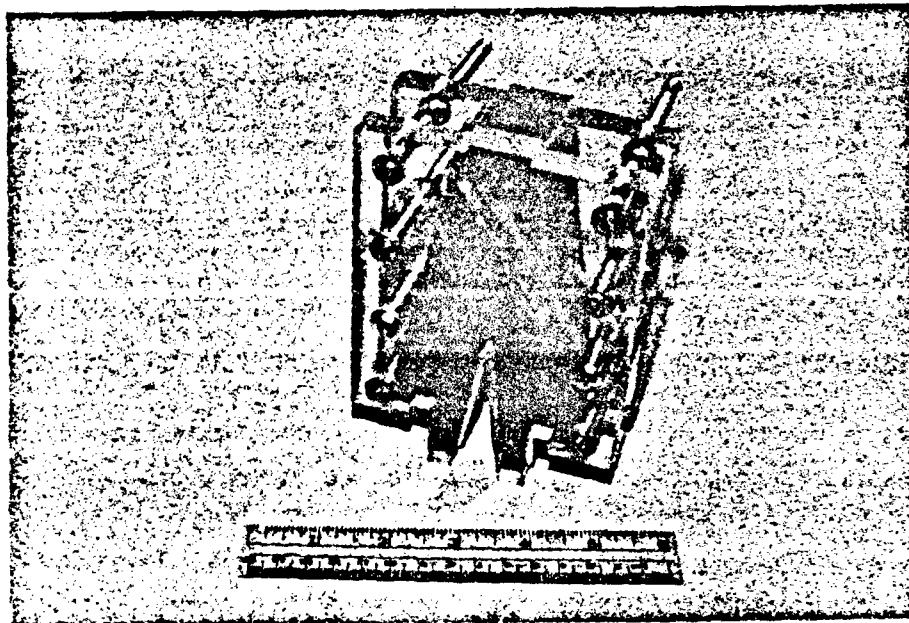
Fig. 13 Photograph of the Propellant Sample Clamped Between
Plexiglass Tamplets
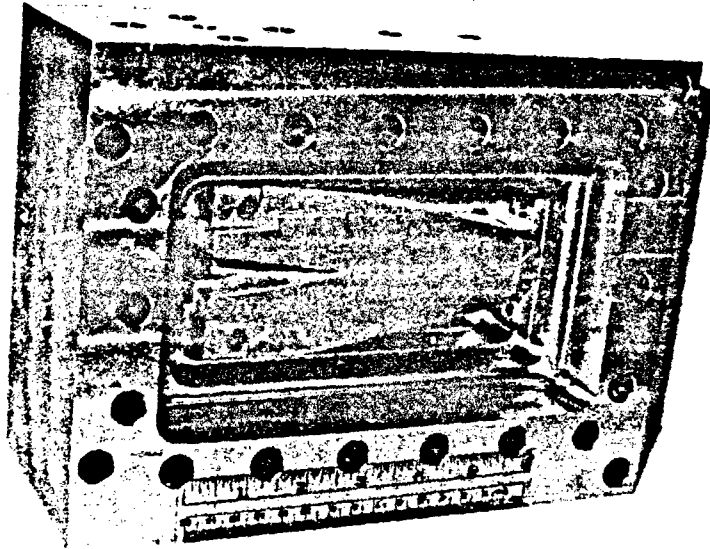
Fig. 14 Photograph of a Propellant Sample Installed in the
Crack Propagation Chamber
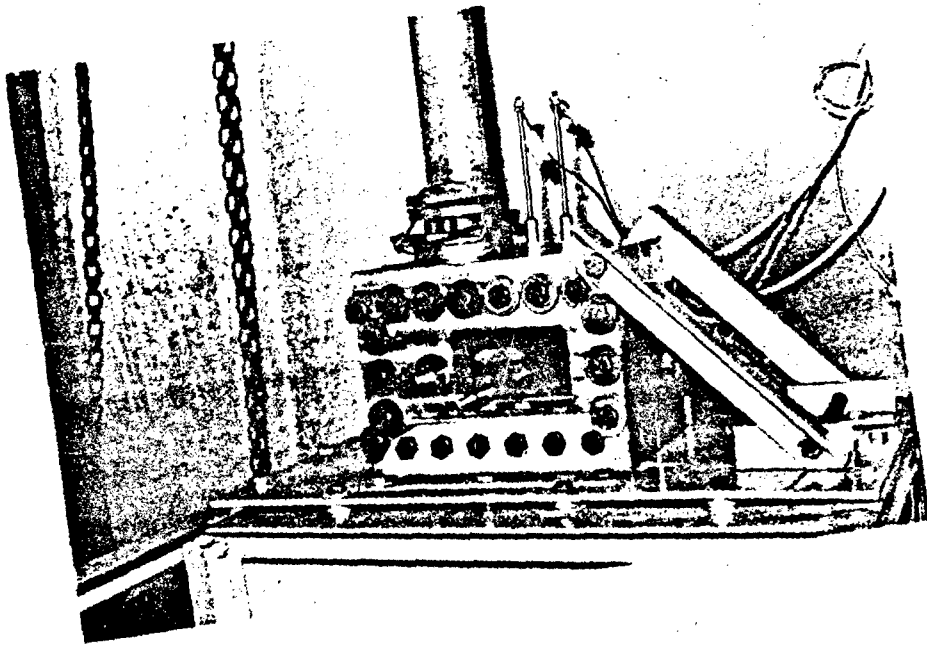
Fig. 15 Photograph of the Assembled Test Rig

cannot be seen in this picture. The product gases from the driving motor flow upward to the main test chamber and a portion of the hot gases enters the crack cavity.

In order to secure the test rig, several angle irons are used to bolt the test chamber tightly to the test frame. The exhausted gases leave the chamber through a long vertical pipeline.

3.3 Sequence of Events

During a test firing, the propellant sample cavity is pressurized by high temperature and high pressure gases produced from the small driving motor. The above-mentioned propellant sample configuration permits significant displacements of the crack walls, so that high stresses and strains can occur at the tip region leading to crack propagation. An electric primer is used to ignite the boost propellant and the igniter charge. The combustion product gases from the driving motor flow through a multi-perforated nozzle into the main chamber and enter into the crack cavity. The propellant surfaces in the cavity become ignited shortly after the penetration of the hot gases. The gases generated from the burning crack surface may not be able to leave the cavity area immediately, therefore causing local pressurization, mechanical deformation, and crack propagation and branching. The initial pressurization of the crack cavity is controlled by the mass and energy fluxes of the product gases coming from the driving motor. The pressurization rates generated from the driving motor ranged between 1 and 35 GPa/s, while the maximum observed pressure in the test chamber was 80 MPa.

3.4 Data Acquisition System

The data acquisition system consists of two major parts: a) a pressure recording system and b) an ignition event recording system. Pressure measurements are taken at six locations described previously. The pressure signal from a transducer is sent to a charge amplifier and the amplified signal is recorded on a transient waveform recorder and a high-speed magnetic tape recorder. A high-speed 16-mm motion picture camera is used to film the ignition event in the chamber. The maximum framing rate of the camera is 44,000 pictures per second. The detailed discussion of the data acquisition system was presented in the last annual report and hence it is not repeated in this report.

3.5 Experimental Results

In order to study the effect of pressurization rate and sample geometry on crack propagation processes, other variables such as propellant type, initial temperature, initial angle of the triangular cavity, were held constant in this investigation. Three sets of p-t traces obtained in test firing No. DNCP2-14, DNCP2-15, and DNCP2-13 under initial pressurization rates of 10.4, 8.3 and 33.4 GPa/s are shown in Figs. 16, 17, and 18, respectively.

Figure 16 shows the set of p-t traces with the medium pressurization rate at the crack tip. These traces were recorded at two different sampling rates (2.5 µs for the initial uprising portion of 7.5 ms and 2.5 ms per sample for the remaining portion) resulting in an abrupt change in pressure traces near pressure spikes. The rapid pressure decay after the peak pressure is due to the rupture of the bursting diaphragm. As can be seen from Fig. 16, the first discernible pressure rise at the sample center G4 (which is beyond the initial crack tip) occurs later than that at the crack tip G3.
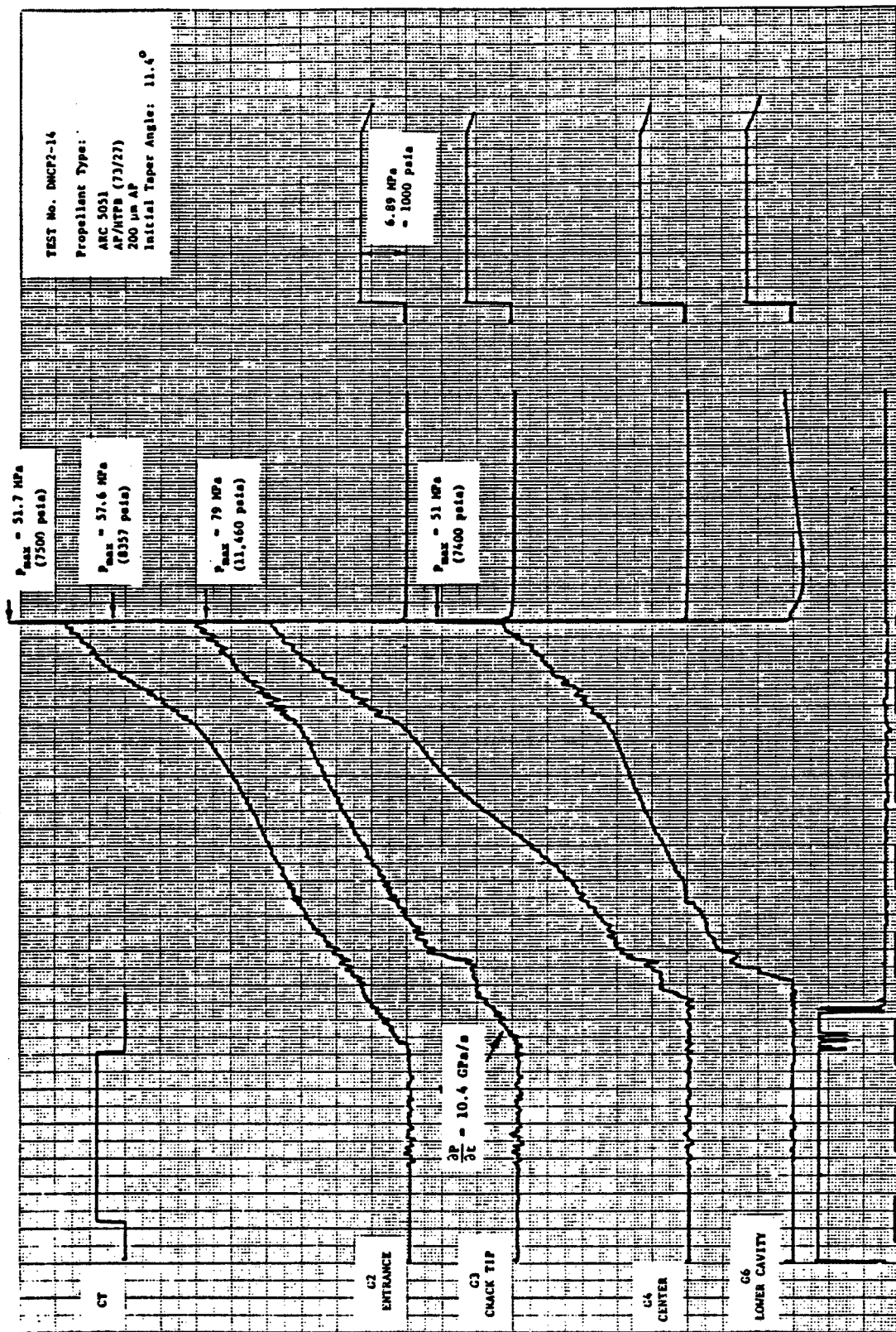
FIG. 16 EXPERIMENTAL DATA OF CRACK PROPAGATION TEST FIRING NO. DNCP2-14
(FRAMING RATE = 16,000 PPS)

TEST No. DNCP2-15

Propellant Type:

ABC 5051
AP/HTPB (73/27)
200 μm AP
Initial Taper Angle: 11.4°

P_{max} = 62.1 MPa
(9004 psia)

6.89 MPa
= 1000 psia

P_{max} = 65.8 MPa
(9536 psia)

P_{max} = 49.4 MPa
(7156 psia)

P_{max} = 72.6 MPa
(10524 psia)

$\frac{\partial P}{\partial t}$ = 8.3 GPa/s

CT

G2
ENTRANCE

G3
TIP

G4
CENTER

G6
LOWER CAVITY

PV
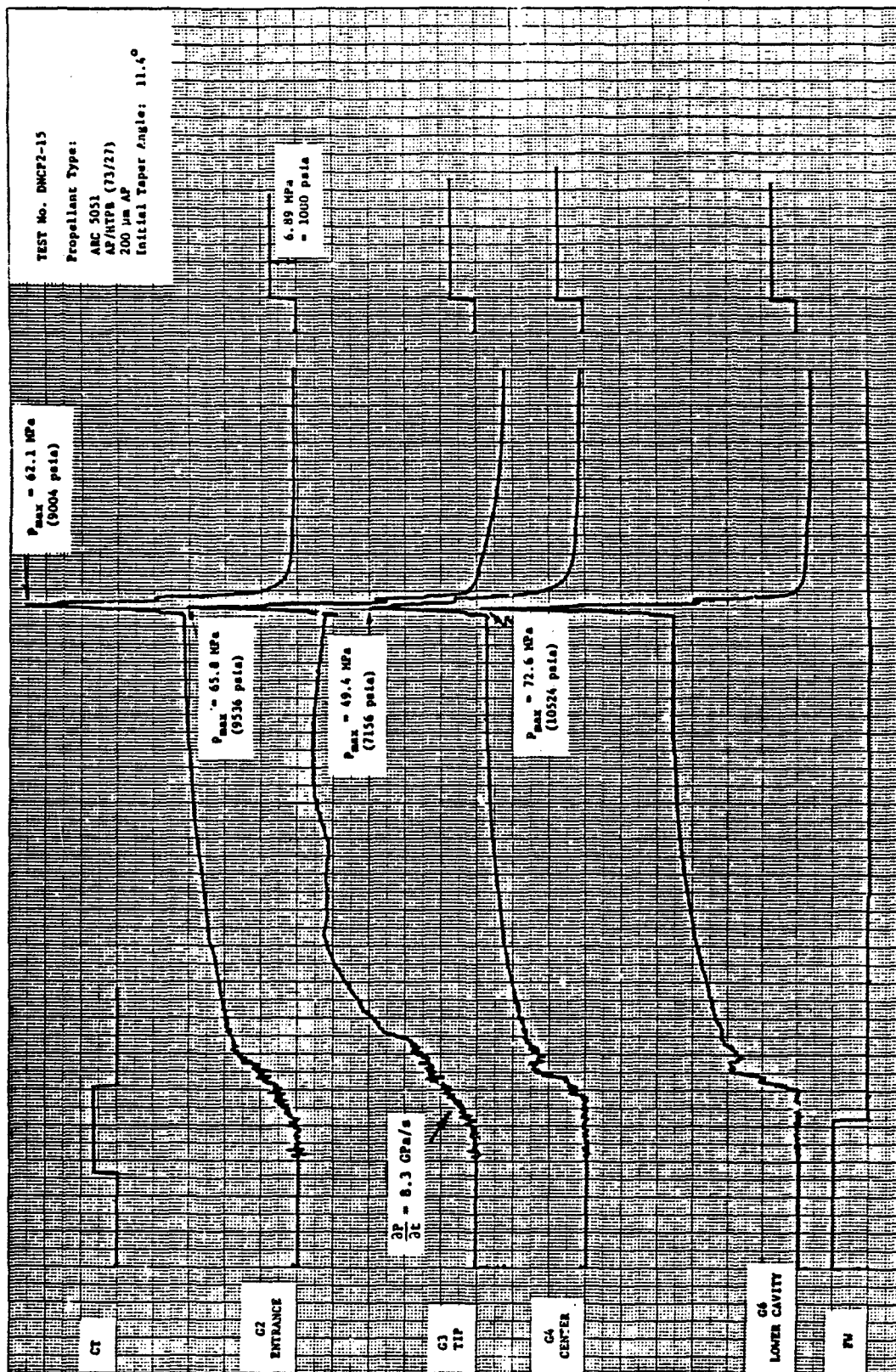
1ms PICTURE 1   PICTURE 32   PICTURE 64

FIG. 17   EXPERIMENTAL DATA OF CRACK PROPAGATION TEST FIRING NO. DNCP2-15
(FRAMING RATE = 16,000 PPS)
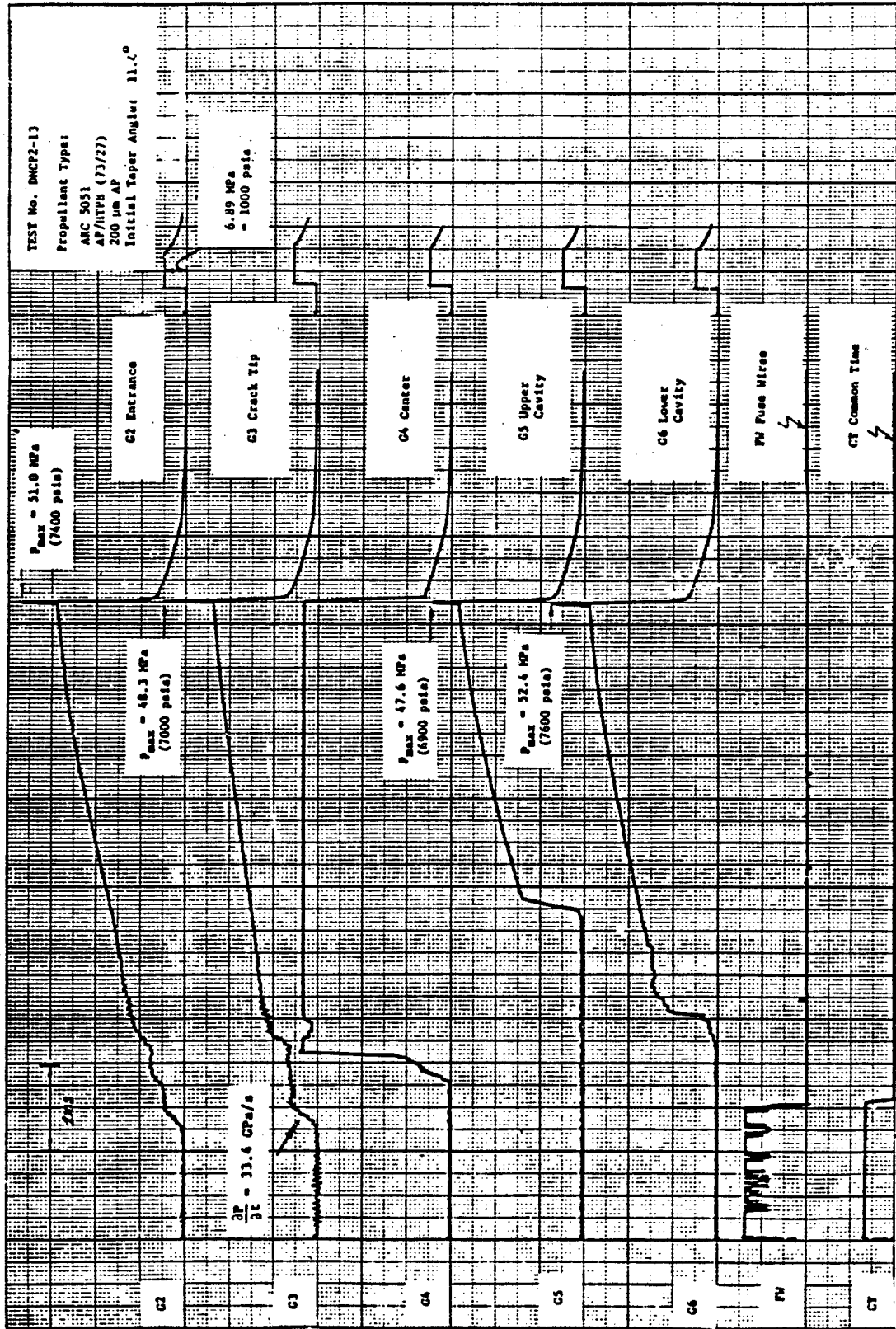
FIG. 18 EXPERIMENTAL DATA OF CRACK PROPAGATION TEST FIRING NO. DNCP2-13
(FRAMING RATE = 32,000 PPS)

However, the pressure and the pressurization rate of G4 is higher than those of G3. This higher pressure and pressurization rate at G4 is believed to be caused by large specific surface area generated by microstructure damage of the propellant during crack propagation and branching as seen from the high-speed film to be discussed in a later section.

The pressure-time traces in Fig. 12, corresponding to the lower initial pressurization rate, show that the maximum pressure near the center of the sample is lower than that at the tip. After the initial time period of 3 ms, the pressurization rates at G4, G3, and G2 become almost the same. Comparing Fig. 17 (low initial pressurization rate) with Fig. 16 (medium initial pressurization rate) it can be seen that the pressurization rate is increasing in the downstream direction for the experiment with the higher initial pressurization rate.

Figure 18 reveals an important phenomenon occuring in the firing test with the highest initial pressurization rate at G3. The pressure at the center of the sample rose so abruptly and became saturated in a very short time. From this figure, one can expect that the center of the sample must be burning severely in order to have such high gasification and pressurization rates. Comparing p-t traces of Fig. 18 with those of Figs. 16 and 17, it can be observed that the response of G4 is steeper for higher initial pressurization rate at G3. One explanation for this observation is the increased degree of damage near the crack tip region due to higher pressure loading. This damage can contribute significantly to provide a larger burning surface area and consequently increase the local mass burning rate.

In tnese tests, the fuse-wire signals shown on Figs. 16, 17, and 18 were not helpful in giving information for the arrival of crack front. This is due to the fact that fuse wires were mounted too close to the tip where large deformation occurred. New locations for fuse wires in the upper part of the propellant sample are planned for future firing tests.

The crack propagation event was recorded by means of high-speed photography. Two typical film records corresponding to test firings DNCP2-14 and DNCP2-15 are shown in Figs. 19 and 20, respectively. As one can see from these films, hot gases from the driving motor illuminated the crack cavity and outlined the crack walls. In these figures, each vertical column of light is the outlined crack at a different time. The event proceeds from left to right, with a time interval of 59 µs between consecutive pictures. The event shown in Fig. 19 is described as follows.

Picture	Time, µs	Observations and Interpretation
1	0	Hot igniter gas starts to enter the triangular cavity.
2-5	59-236	A typical mode I crack propagation occurs with the crack tip displacement in the axial direction. Near the crack tip a small triangle is formed indicating the existence of only one crack. The dark horizontal line is due to the view blockage of the window retainer material between the two viewing ports.
6-7	295-354	A dramatic change takes place in the propagation mechanism. Two spherical regions

Picture No.

$\leftarrow \Delta t = 59 \ \mu s \rightarrow$
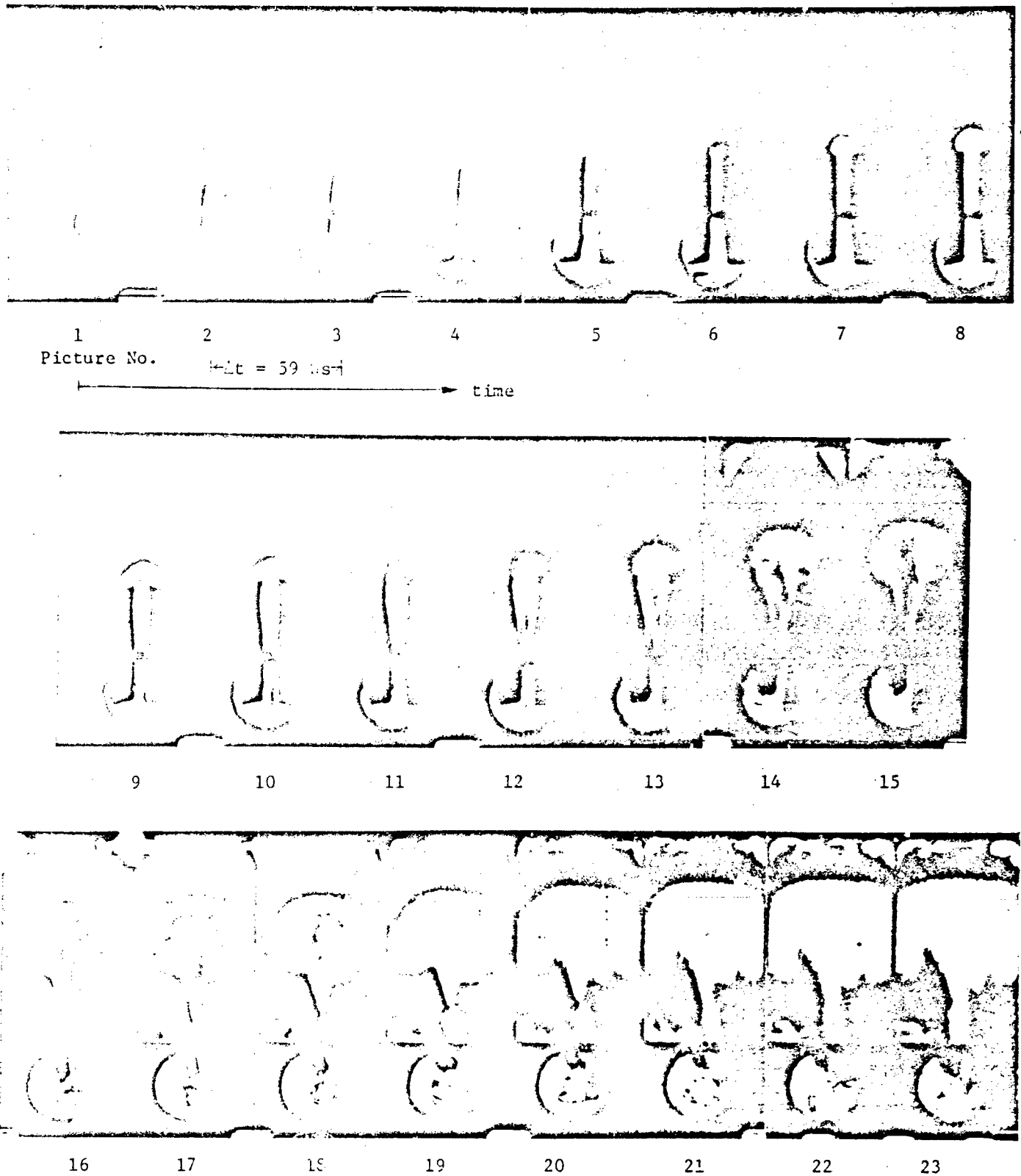
time

Fig. 19 Motion Pictures for DNCP2-14 Firing Test

Picture No.

$\vdash \Delta t = 59 \ \mu s \dashv$
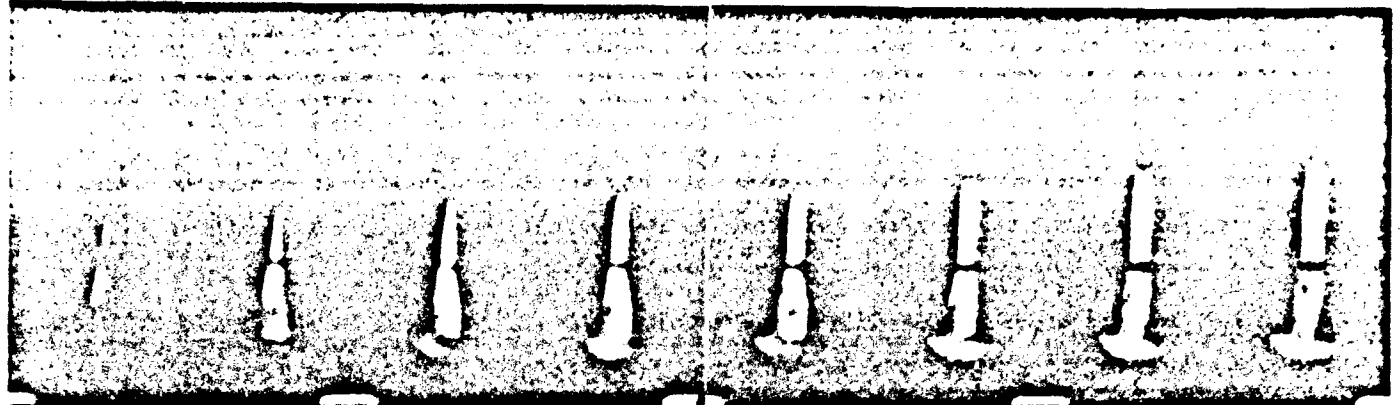
time

1 2 3 4 5 6 7 8
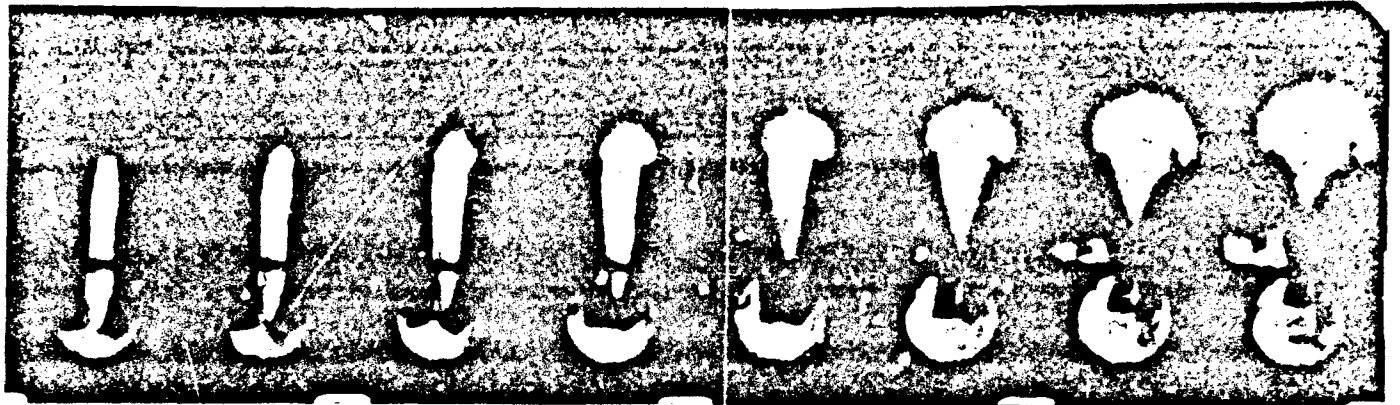
9 10 11 12 13 14 15 16
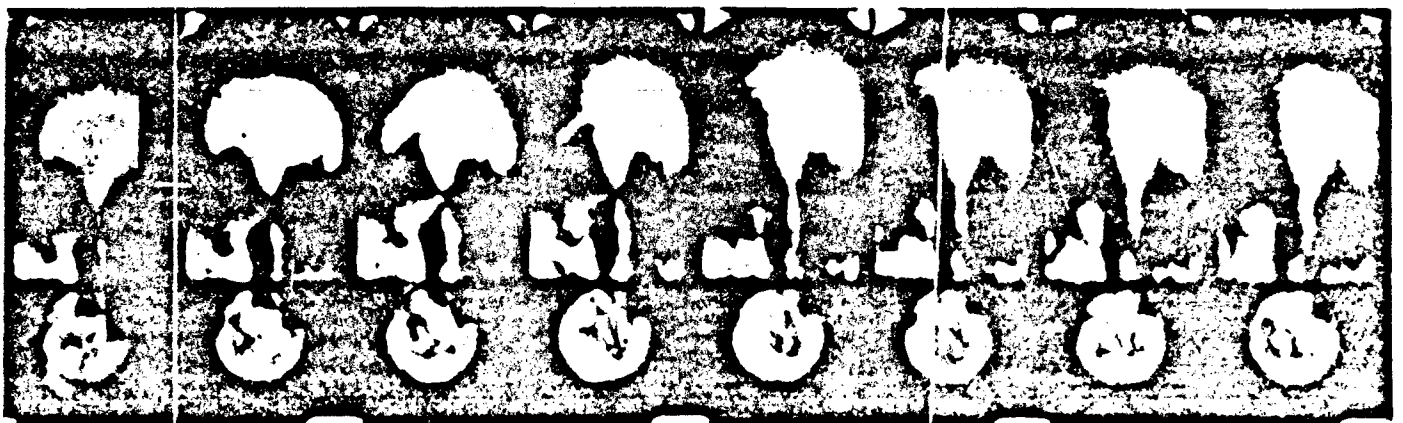
17 18 19 20 21 22 23 24

Fig. 20 Motion Pictures for DNCP2-15 Firing Test

are developing near the tip and a significant enlargement of the luminous volume occurs. This shows that branching starts at two different places located near the shoulders of the luminous volume and propagates outward.

8-10	413-531

A mushroom-shaped luminous region is developing near the tip of the crack. In the meantime, the crack walls became almost parallel, and the crack tip itself loses its definite triangular shape and became a jagged horizontal line. One explanation for the mushroom-shaped region and the corresponding change in crack geometry is the microstructure damage which permits the penetration of hot gases into the damaged region near the crack tip.

11	590

A reduction of the mushroom-shaped region can be observed. The severe burning near the burning near the crack tip can cause mechanical compression of the material ahead of the jagged horizontal front. This compression may lead to the close up of some micropores, and hence reduce the luminosity of the mushroom-shaped region.

12-13	649-708	The continued burning and gas penetration at the tip front enlarges the luminous zone.
14	767	Some pores of the burning propellant are extended far enough to allow the penetration of the flame to the free volume regions, causing illumination of the outer boundary surfaces of the sample. Large mechanical deformation of the outer boundaries is observed.
15-21	826-1180	Severe burning is taking place near the center of the test sample. The mechanical deformation becomes so large that the free volumes almost disappear. The mushroom-shaped region continues to enlarge at the center of the sample. The total mass burning rate increases significantly with time.

Figure 20 shows the crack propagation event under a lower initial pressurization rate at G3. The general sequence of the event is similar to that of Fig. 19. The major differences between the two events are:

1) The bifercation of the spherical regions starts much later for the lower pressurization case. The spherical regions are not as luminous as those shown in Fig. 19.

2) The development of a mushroom-shaped region also occurs at a later time.

3) The flame penetration through the sample into the free volume regions also occurs at a later time.

4) Opposed to Fig. 19, unsymmetric mushroom-shaped regions are observed. This is probably caused by the close up of some micropores due to uneven mechanical deformation.

The relationship between vertical crack-tip displacement and chamber pressure was achieved by combining the pressure-time traces and the displacement vs. time observations. Examination of this relationship illustrates the influence of the pressurization rate and crack sample geometry on crack propagation velocity. Displacement vs. pressure curves for three tests having the same initial sample geometry, but different pressurization rates, are shown in Fig. 21a. A linear approximation was used for the data points obtained in each test. It is obvious from this figure that the tests resulted in three linear relationships between displacement and pressure, and that the slopes of the displacement vs. pressure curves decrease with increasing pressurization rate. Considering that only pressurization rate and sample geometry were varied, the relationship between the slopes of the displacement-pressure curves and these parameters can be generally written as:

$$\frac{ds}{dp} = F(\frac{dp}{dt} \text{ , geometry)} \tag{31}$$
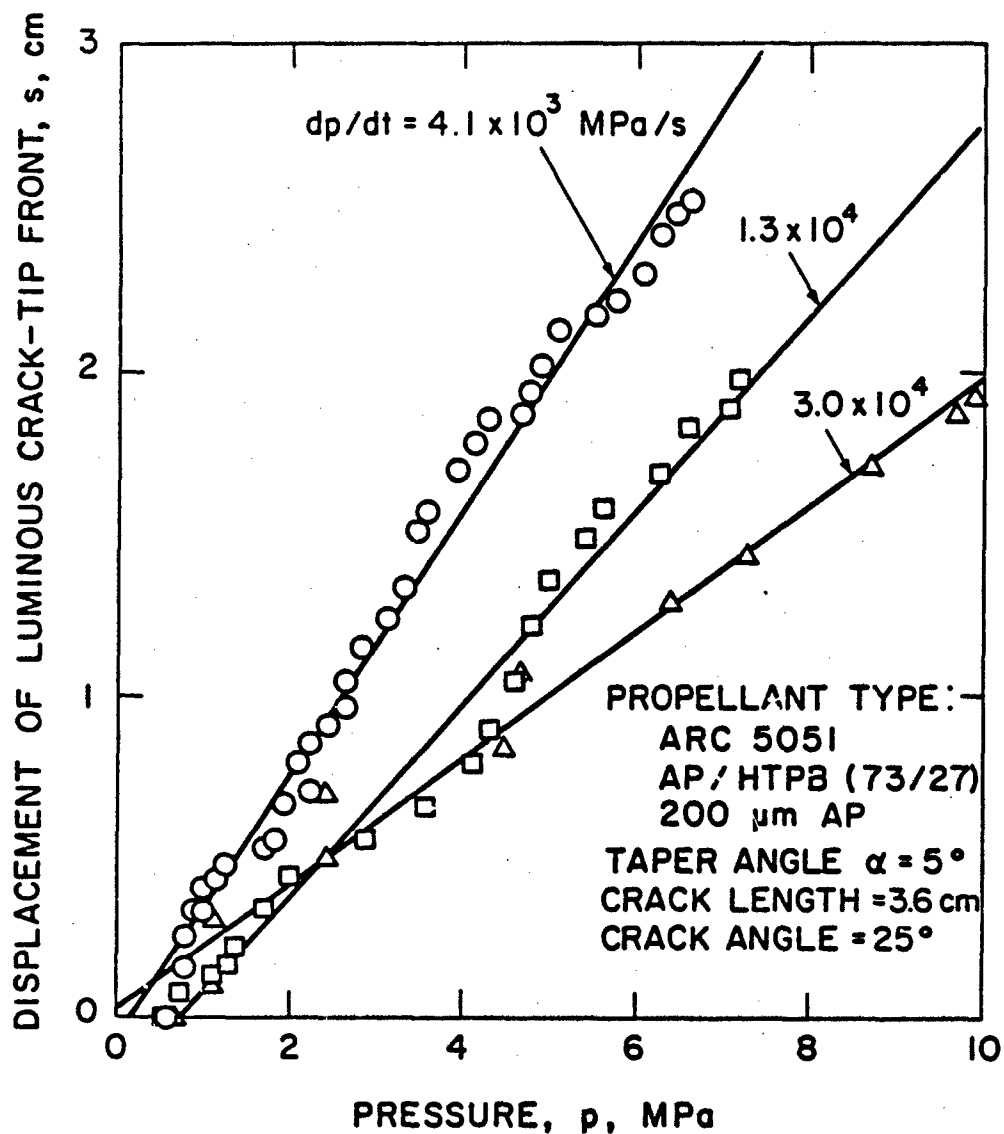
Fig. 21a Measured Crack Tip Displacement vs. Chamber Pressure for
Crack Samples with the Same Initial Geometries

For the tests shown in Fig. 21a, where the geometry was held constant, the above expression reduces to the following:

$$\frac{ds}{dp} = f(\frac{dp}{dt}) \tag{32}$$

This function was approximated by a power law, whose coefficients were determined by a linear approximation of the log-log plot of ds/dp versus dp/dt for the tests with the fixed geometry. The function was found to be closely approximated by the following relationship

$$\frac{ds}{dp} = 0.086 \ (\frac{dp}{dt})^{-0.363} \tag{33}$$

The above equation was used to derive the following experimental correlation relating crack propagation velocity and pressurization rate:

$$\frac{ds}{dt} = V_c \ (m/s) = 0.086 \left[\frac{dp}{dt} \ (MPa/s) \right]^{0.637} \tag{34}$$

It can be seen that the derived correlation is in agreement with the aforementioned observation that the crack propagation velocity increases as the chamber pressurization rate becomes higher.

To examine the influence of different propellant sample geometries on observed crack propagatoin velocities, three crack-tip displacement vs. pressure curves are plotted in Fig. 21b. During the three separate tests with different sample geometry, the pressurization rate was held constant, approximately 15,000 MPa/s. The sample geometry differed in the taper angle of the external surfaces of the propellant sample, which changes the free volume regions of the test chamber. The sample with the maximum free volume corresponds to the curve with the highest ds/dp shown in Fig. 21b. Considering the fact that these tests were conducted under the same average pressurization
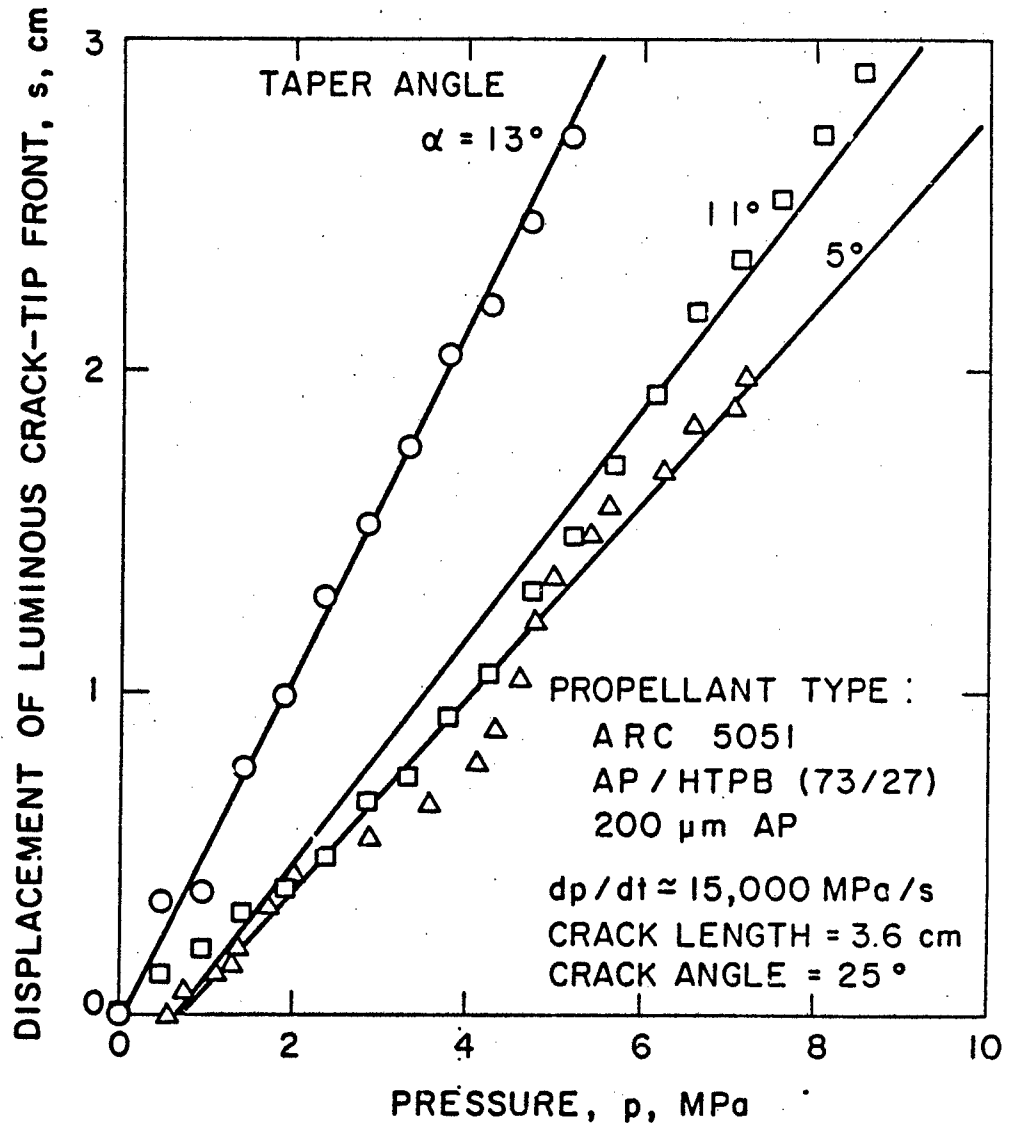
Fig. 21b Measured Crack Tip Displacement vs. Chamber Pressure
for Crack Samples with Different Initial Geometries
and Constant Pressurization Rate

rate, it can be easily found that the steeper the slope of the curve in Fig. 21b, the higher the average crack propagation velocity.

Combined data obtained from several tests with different geometries and pressurization rates are shown in Fig. 22. The solid line is the correlation given by Eq. (34), and the dashed lines represent the similar relationships at different taper angles. Since the data points of these curves are limited, the main usefulness of Fig. 22 is to display the qualitative trends of the effect of dp/dt and taper angle on crack propagation velocity.

In order to explain the crack propagation velocity dependence on pressurization rate and sample geometry, two common propagation mechanisms were examined. The first mechanism considers that the crack is propagating at its terminal velocity, V_t, which is approximately equal to one-third of the speed of sound in the propellant as suggested by Swanson.[33] As the pressurization rate is increasing, the dynamic and relaxation moduli of the viscoelastic propellant are also increasing. This results in a higher terminal velocity in the propellant, according to the following formula:

$$V_t = \frac{1}{3} \sqrt{E/\rho}_s \tag{35}$$

where E is the dynamic modulus and ρ_s is the density of the propellant sample. Over the range of pressurization rates tested, changes in moduli are approximately 10%; therefore, these small changes in moduli do not result in significant increase in crack propagation velocity as measured in this work. This observation has been made by Gent and Marteny[34] in their work with natural rubbers under rapid loading rates. The first mechanism does not consider any changes in the crack propagation velocity due to different sample geome-
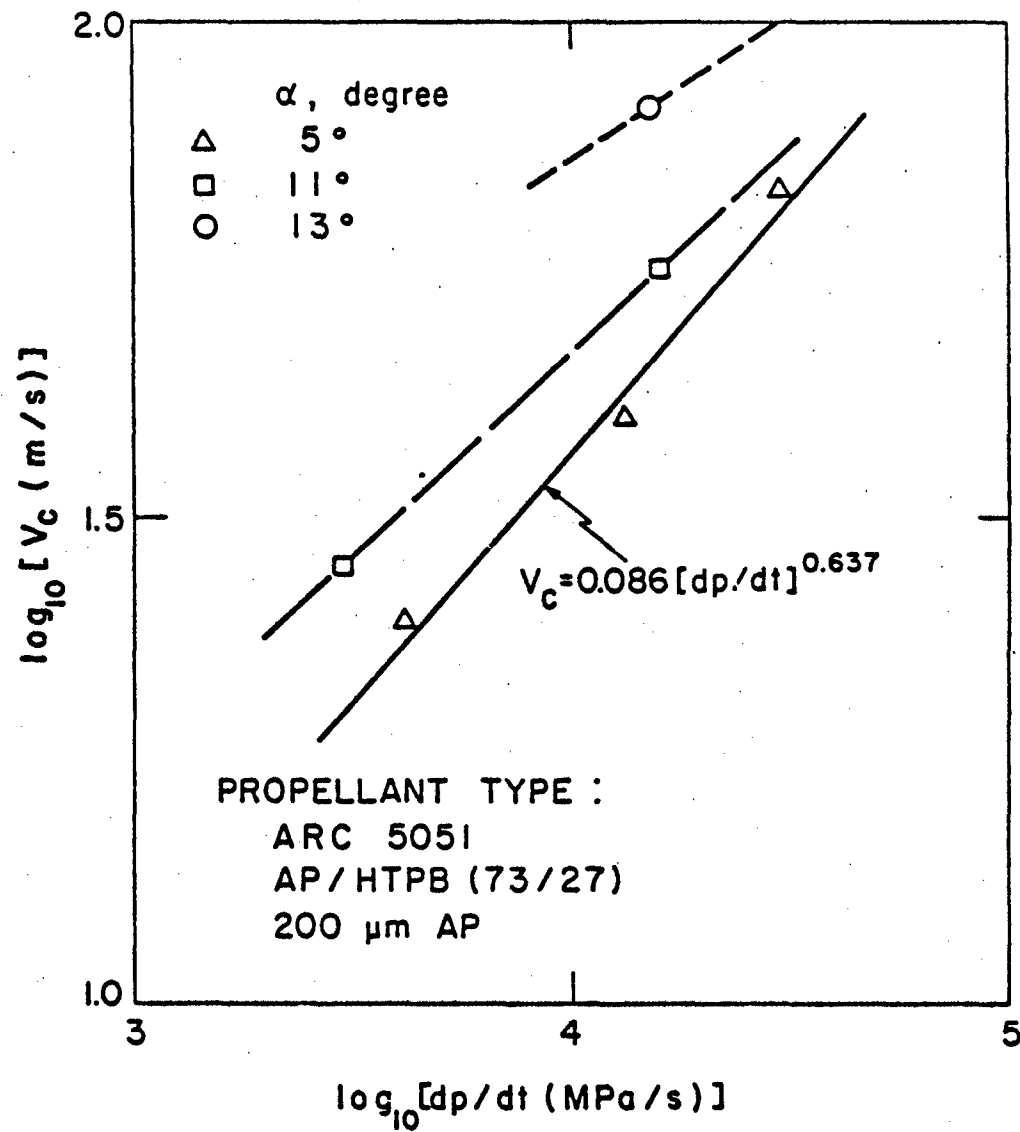
Fig. 22   The Combined Effect of Pressurization Rate and Sample
Geometry on Crack Propagation Velocity

tries.

The second crack propagation mechanism to be discussed considers that the velocity of the running crack is limited by the speed of the deforming crack contour. In order to have crack propagation, a sufficient stress state must be maintained at the crack tip. For geometries tested in this study, the large deformation of the crack cavity observed from the high-speed films is believed to provide the high stress distribution near the crack tip. The crack tip front shown by the luminous contour seems to be limited by the rate of deformation of the crack cavity walls. However, actual crack tip propagation velocity may exceed the observed velocity obtained from the displacement of the luminous front. The microstructural damage of the propellant ahead of the luminous front may not be seen from high-speed films. Some of the micro cracks are submerged beneath the surface, and also there is a time lag for the gas to penetrate these micro cracks.

The quasistatic application of this mechanism would predict that the crack propagation velocity is proportional to the first power of pressurization rate. This is because of the fact that a given static pressure load would correspond to a certain displacement of the crack contour. This should result in the three curves in Fig. 21a coalescing into one. However, the experimental results of Fig. 21a show a significant dependence of ds/dp on dp/dt. The changes of slope at different pressurization rates shown in this figure are believed to be caused by the delay of the sample leg displacment at higher loading rates due to the effect of inertia during the acceleration of the sample mass.

From the above, one can deduce that the dynamic application of this mechanism would show weaker dependence of V_c on dp/dt than the quasistatic one. The exponential coefficient of dp/dt in the dynamic application would be lower than one which is in agreement with the experimental results of Eq. (34).

Similarly, the changes in slope at different geometries shown in Fig. 22 are believed to be caused by the decrease in resistance of the sample leg displacement for larger taper angles. This implies that the greater the free volume, the quicker the response of the propellant sample to the pressure loading and consequently the higher the crack propagation velocities. The approximate magnitudes and the tendencies of the curves in Fig. 21a and 21b were simulated by solving analytically a very simplified model consisting of a Voigt-Kelvin parallel spring-damper element in series with a point mass. The coefficients for the system were approximated from results of the static finite element analysis and sample geometry. The results of the above simple analysis produce qualitatively the same changes in ds/dp, due to the different loading rates and geometries.

It is believed that at much higher pressurization rates than those tested in this study, higher crack propagation velocity would be reached. Under these conditions, the influence of sample geometry would be less significant and the first crack propagation mechanism would be important.

Swanson[33] and Gent and Marteny[34] measured crack propagation velocities in inert propellant (Solithane 113) and rubber, respectively. Swanson reported the highest observed velocities of approximately 40 m/s, while Gent and Marteny[34] measured highest velocities of 80 m/s in specimens with no pre-

imposed strains in the crack direction. It is interesting to note that their measured highest velocity is in the same order of magnitude as the observed luminous front propagation velocity in burning solid propellants. The actual crack propagation velocity can be substantially higher than that of the luminous front for reasons stated above.

3.6 Finite Element Analysis

An analytical stress analysis of the propellant sample was performed using a finite element techique. The objectives of this analysis were: a) to understand how the sample would deform in a cold environment under uniform internal pressure loading; b) to predict the way in which the propellant sample fractures; and c) to estimate the contribution of mechanical deformation in the overall measured crack tip displacement.

The propellant sample geometry modeled was similar to that described in Section 3.2. A finite radius of 1.78 mm was selected at the crack tip in order to use a manageable number of mesh elements to study the local stress and strain distributions. The finite radius approximation reduces the accuracy of the solution near the tip. However, the solution is useful to have a qualitative representation of the mechanical deformation of the propellant sample near the crack tip.

The employed finite element grid was generated by using an interactive mesh generation program and the grid pattern was shown in the last annual report. The material properties assumed for the model where an elastic modulus, E, equal to 55 MPa and Poisson's ratio, v, equal to 0.5. Even though elastic behavior was considered, the viscoelastic character of the sample was

approximated by substituting the relaxation modulus for the elastic modulus. According to the correspondence principle, the selection of the relaxation modulus was based upon the test pressurization rate and initial temperature of the propellant. This is a commonly used procedure in solid propellant grain deformation analysis.

A static analysis of the described model was solved with a nonlinear finite element code (ABAQUS).[35] The program permitted incompressible material behavior and large deformations which were needed in order to solve the problem. The obtained results are discussed in terms of the following three subject areas of interest: a) displacement of the crack tip along the crack centerline; b) contour deformation; and c) stress and strain distribution near the crack tip.

a) Crack Tip Displacement

In terms of crack tip displacement, the pressure loading on the inner crack walls resulted in a mechanical displacement along the crack centerline. The calculated vertical displacement was due to the fact that the free boundaries of the sample allowed for horizontal expansion. The displacements of the crack tip node were determined for several pressurization rates, and the calculated results indicated the nonlinearity of the problem. The results of mechanical displacement vs. pressure can be easily converted to displacement vs. time data, assuming that the pressure-time relationship is given and the quasisteady assumption is valid.

Two mechanical displacement curves obtained in this way are shown in Fig. 23; one corresponding to a low pressurization rate of 3,000 MPa/s and
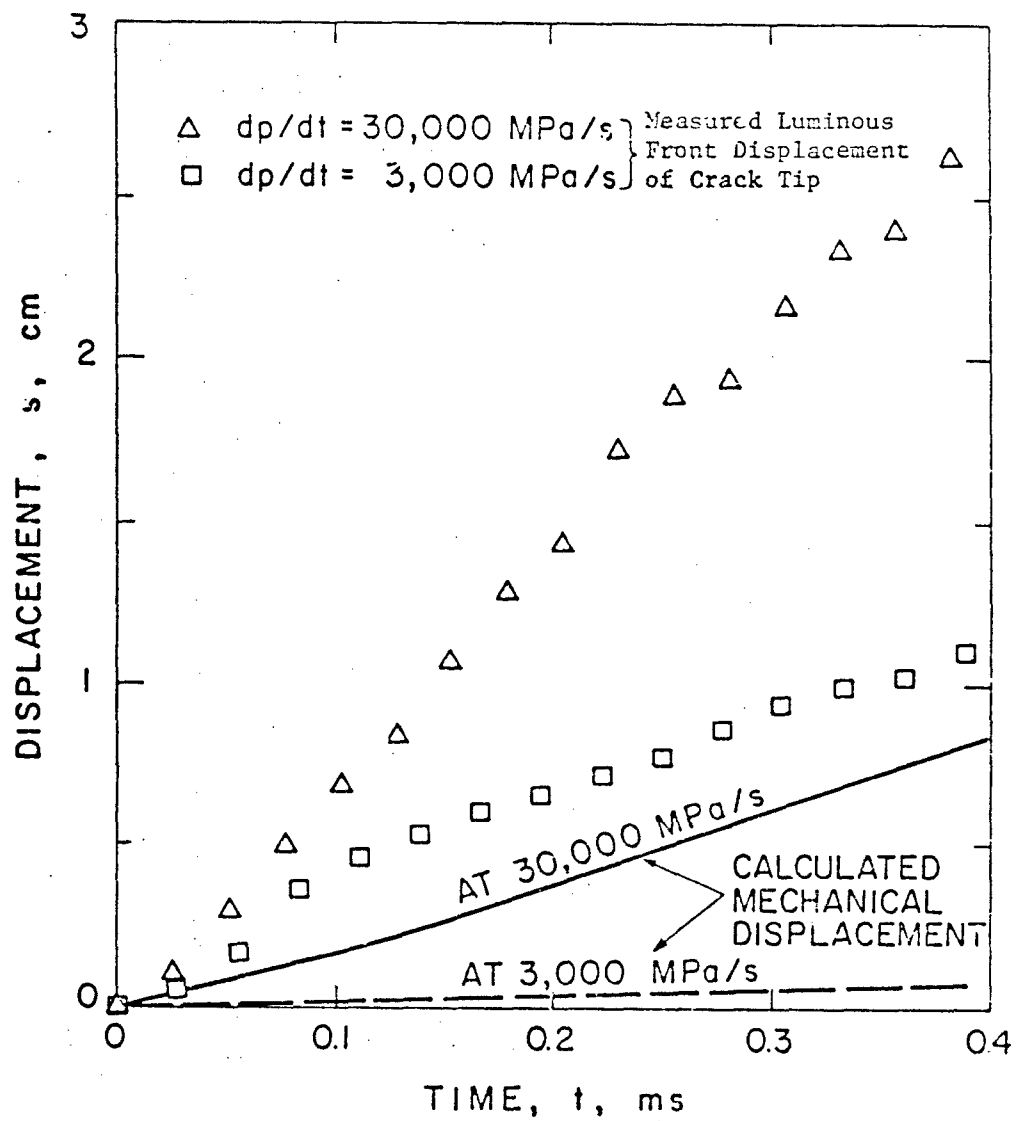
Fig. 23 Calculated Mechanical Displacement and Measured Luminous
Front at the Crack Tip

the other to a high pressurization rate of 30,000 MPa/s. In order to determine the contribution of the mechanical deformation to the overall measured luminous front displacement at the crack tip, the experimentally observed displacements under these two pressurization rates were plotted in the same figure. In the low dp/dt case, it can be seen that the mechanical displacement was considerably smaller than the overall displacement. On the other hand, in the high dp/dr case, a more significant contribution of the mechanical deformation the overall luminous front displacement at the crack tip can be observed. The conclusion is that the higher the pressurization rate, the larger the contribution of the mechanical deformation to the overall luminous front displacement at the crack tip. In order to determine the accuracy of the above results, it is necessary to examine the quasisteady assumption made in the finite element analysis. A simple lumped-mass analysis demonstrates that time lags due to inertia effects are of the same order of magnitude as the duration of the experiment. Therefore, the higher the loading rate, the larger the errors due to the quasisteady assumption. In addition, the static solution gives an upper boundary of the displacement at a given time, since the inertia effect causes actual displacement to lag behind the calculated value.

b) Contour Deformation

When fracture at the crack tip is not allowed, the mechanical deformation at the crack tip tends to slightly round the original triangular shape of the crack inner wall. However, the calculated crack tip deformation is small, as shown in Fig. 23, when compared with the observed high rates of contour changes from experiments. This implies that the crack propagation

must be caused by fracture. Finite element solution showed that the outer surface of the sample deforms towards the chamber wall as anticipated. However, if no crack propagation is allowed, the finite element solution will show a small amount of deformation of the propellant sample legs toward the chamber wall. If one or more cracks were propagating the leg would be free to deform out towards the chamber wall, creating abrupt changes in the crack cavity contour.

c) Stress and Strain States Near the Crack Tip

In order to understand the mode of failure of the propellant sample, a typical propellant grain failure criterion should be used. An experimentally derived failure envelope, based upon the maximum principal deviatoric stress and the corresponding strain, is a common criterion for determining a loading-rate independent failure of solid propellant grains subject to internal pressurization. According to this criterion, the propellant will begin to crack at the surface near a point where the stress and strain states exceed the boundary of the envelope. The two important characteristics of failure criterion are: 1) failure is dependent upon deviatoric stress and not upon hoop or maximum principal stress; and 2) the criterion is based upon the level of the combined state of stress and strain.

The deviatoric stress contours near the crack tip region are shown in Fig. 24a. This figure clearly shows that the maximum deviatoric stress concentration is near the shoulder of the crack tip radius. Four locations on the crack radius are indicated on the figure as points A, B, C, and D. A plot of the maximum deviatoric stress vs. the corresponding strains for these four points is shown in Fig. 24b. It can be seen that the maximum deviatoric
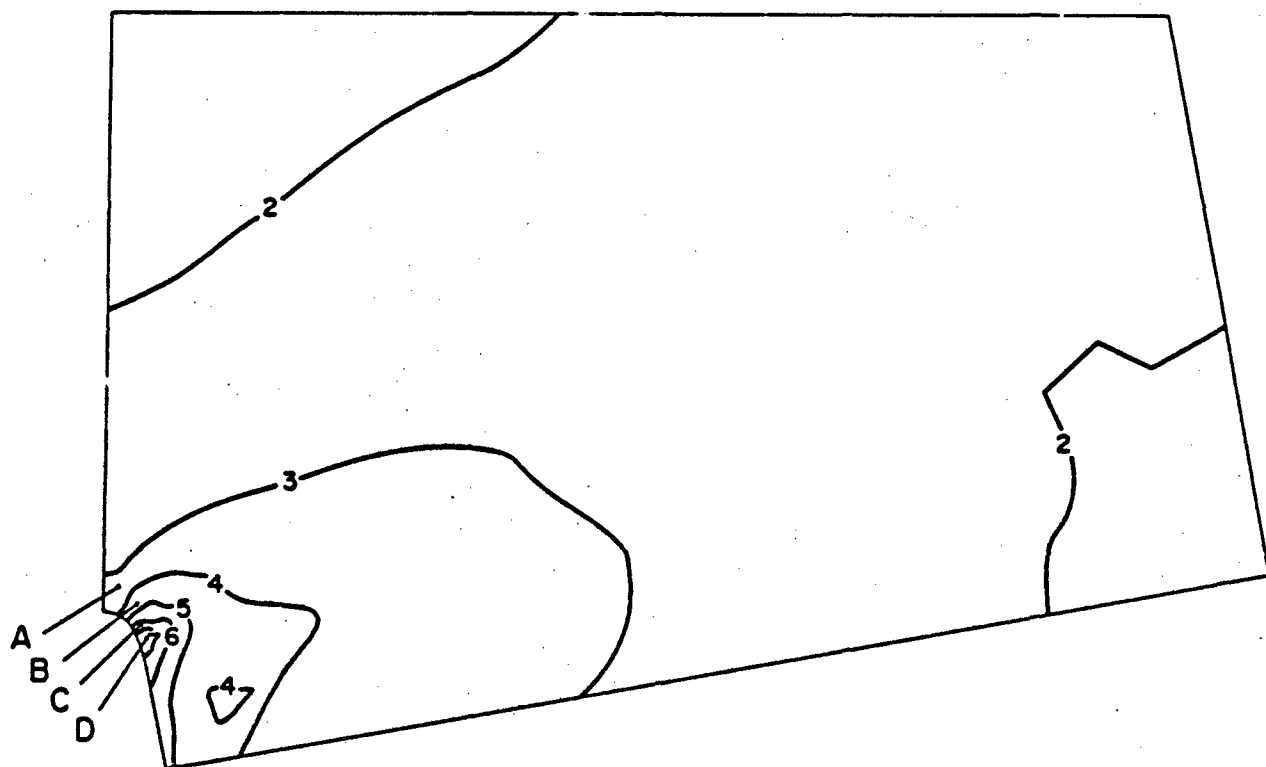
Fig. 24a   Isopleths for Deviatoric Stresses
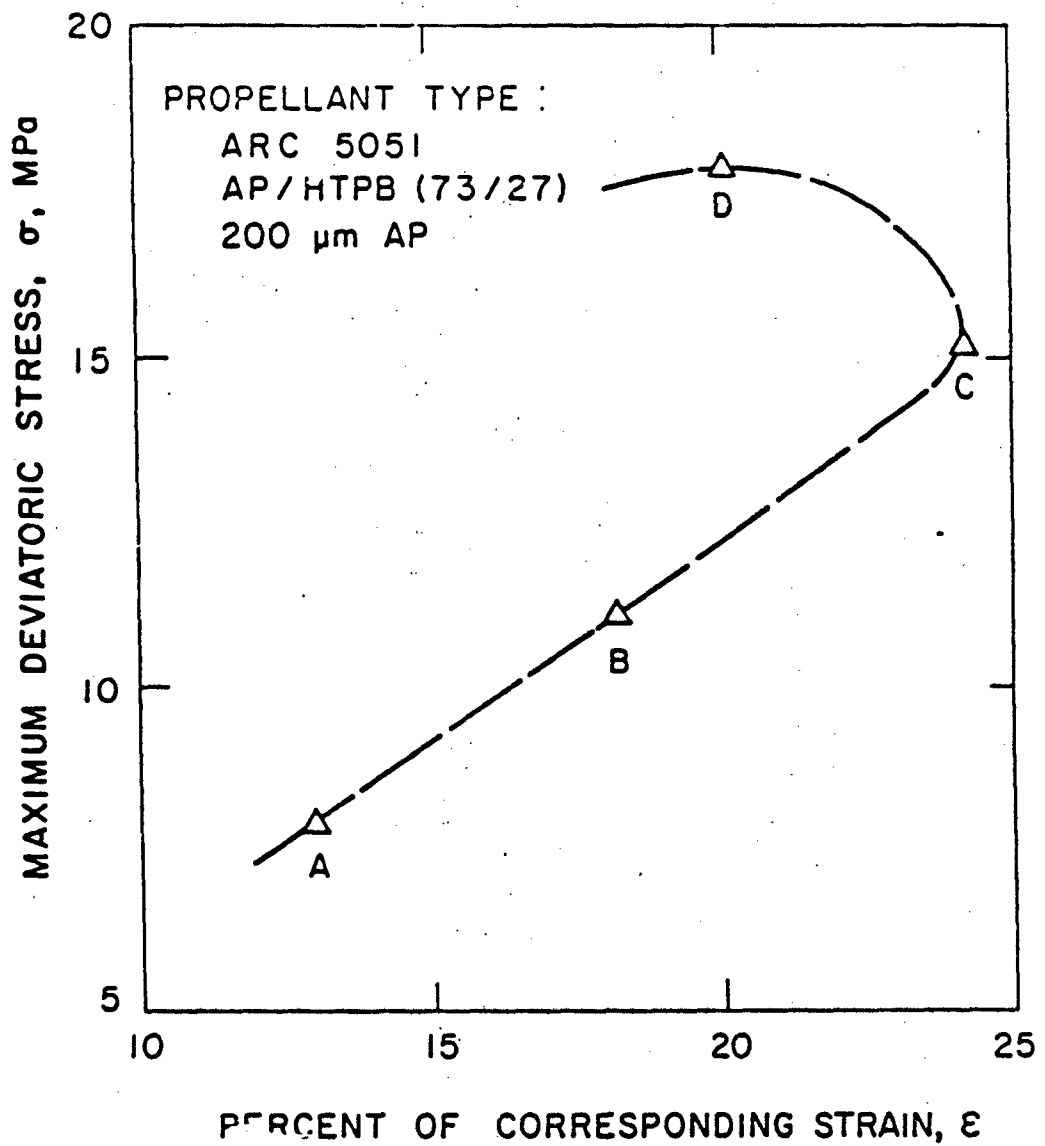
Fig. 24b Maximum Deviatoric Stress vs Corresponding Strain for Crack
Tip Elements at a Pressure of 5.17 MPa

stress occurs at D, on the shoulder of the crack tip, not at the tip zenith. In addition, the maximum strain occurs at C. This implies that, for the geometry and load conditions modeled by the finite element analysis, the most likely area for failure would be in the vicinity of C and D, and not at the crack tip. The symmetry of the model implies that the failure at the shoulder could create two running cracks. In this case, the two cracks would be extremely close together at the onset of failure, because of the small radius of the crack tip. The consideration of dual fracture helps to explain the transition to the two spherical regions and then to a square-shaped geometry as observed on the film during high pressurization rate tests. A multiple fracture of this type would cause dramatic displacement of the crack cavity walls toward the chamber wall.

3.7 Apparent Versus Steady-State Mass Burning Rates

An estimation of the apparent mass burning rate during the crack propagaton can give valuable information about the degree of fracture due to crack propagation and branching, since direct measurement of the burning rate under these conditions is very difficult. One method of obtaining the apparent burning rate is by using the average pressurization rate and initial crack geometry as given in the following. According to mass continuity for the gases in the chamber, we have

$$\frac{dM}{dt} = \dot{m}_b + \dot{m}_{in} - \dot{m}_{out} \tag{36}$$

After a short initial pressurization period, $\dot{m}_{in}$ becomes small and can be neglected. The flow at the exit nozzle can be considered choked because of

high chamber pressure. Using these assumptions together with the perfect gas law, Eq. (36) becomes:

$$\dot{m}_b = \left[\Gamma \frac{P_c A_t}{\sqrt{R\,T_c}} + \frac{V_{ch}}{RT_c} \frac{dP_c}{dt} \right] / \; (1 - \frac{\rho_c}{\rho_s}) \tag{37}$$

where dP_c/dt represents the average chamber pressurization rate. In the above simplified analysis, both T_c and V_{ch} were treated as known constants.

Figure 25 shows the ratio of the computed apparent mass burning rate ($\dot{m}_b$) to the steady-state mass burning rate ($\dot{m}_{b,ss}$) evaluated at the average chamber pressure during crack propagation. It is useful to note that the apparent mass burning rates are about two orders of magnitude higher than the steady-state mass burning rate. The ratio increases for higher pressurization rates. Also, this ratio becomes higher for test chamber having larger free volume for sample deformation.

This apparent increase in the mass burning rate is believed to be mainly caused by the propellant fracture and microstructure damage. This is also supported by the luminous mushroom-shaped region observed above the crack tip. The dynamic (transient) burning effect[36] would also contribute to the total mass burning rate. The relative contribution of these two effects is difficult to determine. This greatly enhanced mass generation rate in highly confined regions could contribute significantly to the onset of detonation.
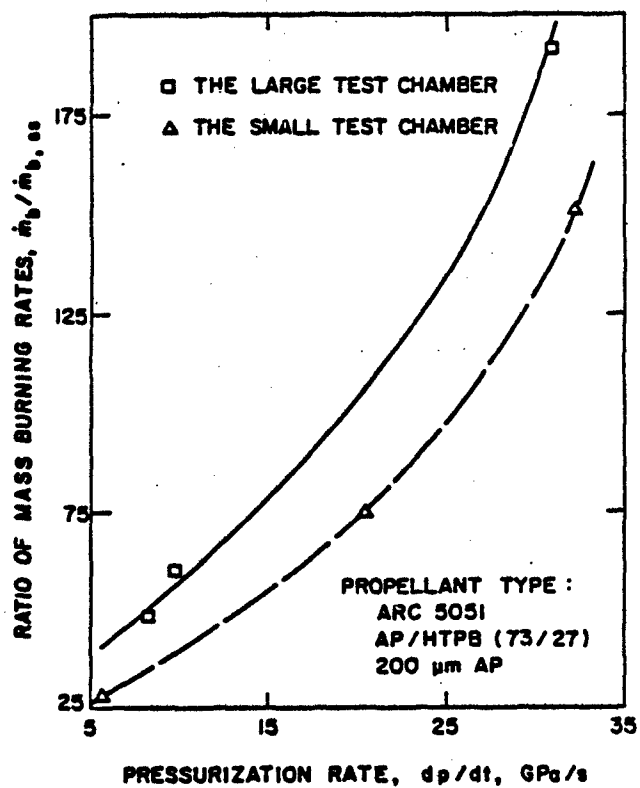
Fig. 25 Effect of Pressurization Rate on
the Ratio of Apparent to Steady-
State Mass Burning Rate during
Crack Propagation

3.8 Designed Modifications for Achieving Interrupted Burning During Crack Propagation

A test rig modification is being performed in order to recover the propellant crack sample from interrupted crack propagation experiments. The propellant sample recovery is important in obtaining direct evidence of the microstructure damage and in achieving better understanding of the crack propagation and branching mechanisms under burning conditions. Careful considerations were given to the test rig modification, so that the sample can be extinguished at a prescribed pressure level by rapid depressurization followed with inert gas injection.

A schematic diagram of the modified test rig and the control circuit for depressurization and inert gas injection is shown in Fig. 26. The procedure to achieve the propellant sample quenching is as follows:

1. As soon as the pressure in the chamber reaches a prescribed value p_1 (shown in Fig. 27), a trigger device will activate the primer located in the second igniter assembly at time t_1.

2. The product gases from the second igniter assembly (see Fig. 25) will pressurize the free space between the two bursting diaphragms and rupture them at time t_1' to cause rapid depressurization of the test chamber.

3. Immediate injection of inert gases at time t_2' upon a time delay of $(t_2'-t_2)$, where t_2 is the time when the inert gas inlet valve was activated. The time distance t between t_2 and t_1 can be preselected and adjusted on a timer.
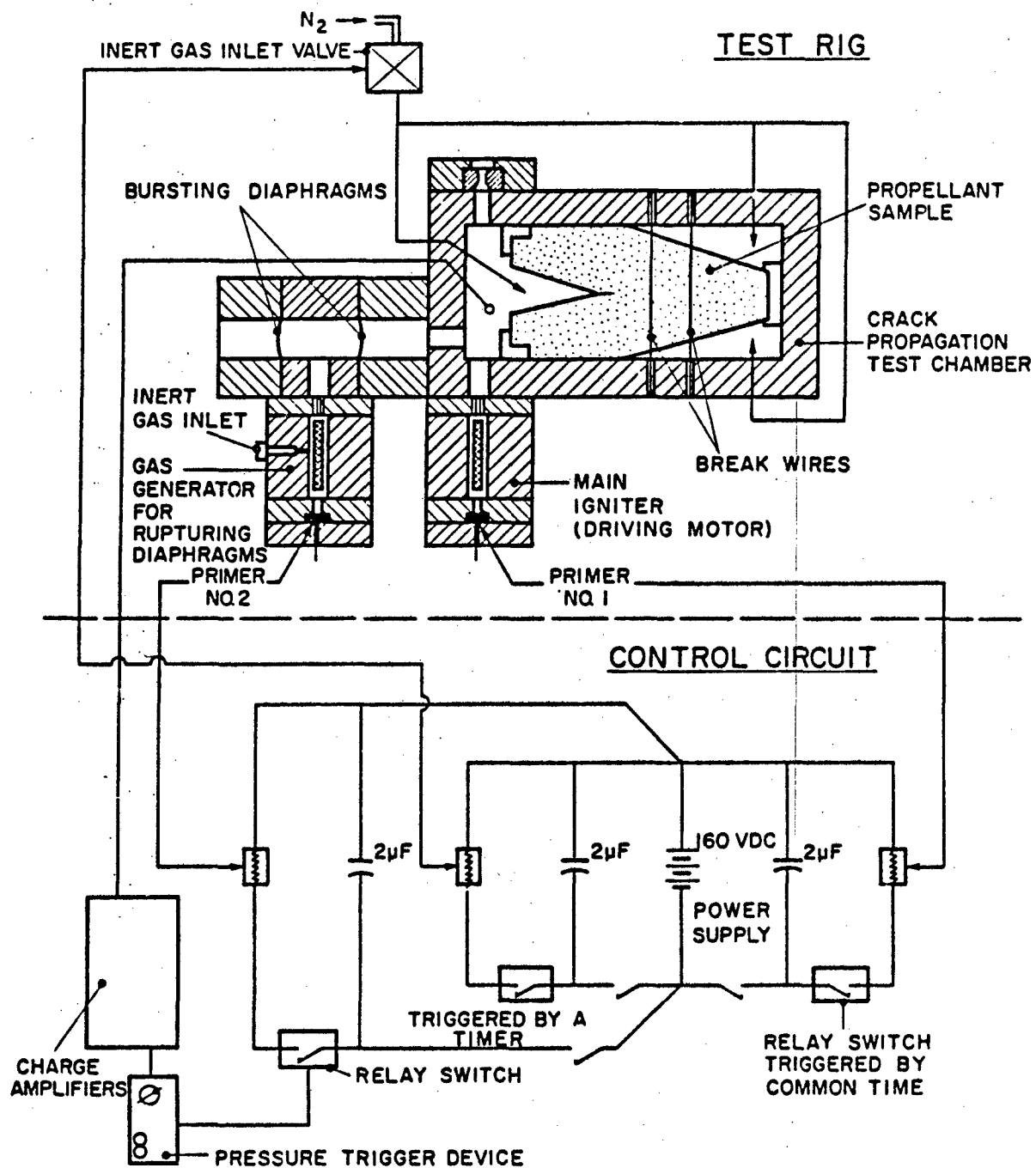
Fig. 26 Modified Test Rig for Sample Recovery
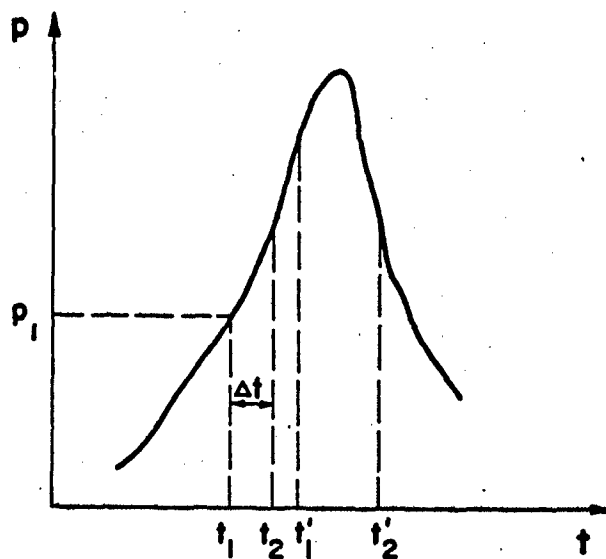
Fig. 27   Triggering Sequence in Reference to
            the p-t Trace of the Test Chamber

4. The inert gas injected into the chamber will quench the inner surfaces of the test chamber and further interrupt the burning of the propellant sample.

The recovered propellant sample will be examined in detail under a microscope to determine the degree of damage encountered during the burning. The recovered sample will be extremely useful for understanding the crack propagation and branching mechanism. One preliminary attempt was made towards this direction without using the above-mentioned circuit; and a small portion of the propellant was recovered. It is believed that larger recovered samples will be obtained after the test rig modification is completed.

IV. SUMMARY AND CONCLUSIONS

Some important observations and conclusions from the tip ignition study are summarized as follows:

(1) Ignition of nitramine composite propellants was studied at rapid pressurization environment. For each test firing, two different propellant samples can be tested simultaneously under the same flow conditions. Three independent data acquisition systems were used for detecting the onset of gas evolution. These systems include the external photodiode system, near-infrared photodiode system, and high-speed filming system. Consistent results were obtained from these systems in determining the onset of gas evolution.

(2) A theoretical model with chemical kinetic is proposed for the ignition of nitramine composite propellants. These kinetic mechanisms and data are helpful in the interpretation of experimental results.

(3) The time required for the onset of gas evolution of nitramine composite propellants decreases drastically as the pressurization rate is increased.

(4) Nitramine composite propellants are much more difficult to ignite as compared to the conventional AP-based composite propellants.

(5) With the same binder, HMX-based composite propellants were found to be more difficult to gasify than RDX-based composite propellants. This is probably due to the fact that both the thermal diffusivity and activation energy for decomposition of RDX are lower than those

of HMX-based composite propellants.

(6) Two HMX-based composite propellants with different binders (CTPB and HTPB) did not show significant differences in the time required for the onset of gas evolution. This is probably due to the fact that the thermal diffusivity effect and the chemical kinetic effect of decomposition of these two binders tend to cancel each other.

Several important observations and conclusions obtained from the crack propagation studies are summarized below.

(1) Luminous front propagtaion velocities of 20 to 80 m/s were observed in a burning propellant crack sample.

(2) For high pressurization rates, the luminous crack tip contour undergoes a highly discernible transition process that a triangular contour develops into a mushroom-shaped region. The evolution of the mushroom-shaped region is believed to be caused by gas penetration and flame propagation into micropores resulting from crack branching.

(3) An experimental correlation, showing strong dependence of crack propagation velocity on pressurization rate and crack sample geometry, has been developed.

(4) The apparent mass burning rate, deduced from the measured p-t traces, was found to be approximately two orders of magnitude higher than the steady-state mass burning rate. This implies that the propellant structure damage due to crack propagation and branching can

significantly increase the burning surface area. This may cause the onset of detonation in strongly confined environments.

V. REFERENCES

1. Price, E. W., Bradley, H. H. Jr., Dehority, G. L., and Ibiricu, M. M., "Theory of Ignition of Solid Propellants," AIAA Journal, Vol. 4 Sept. 1966, pp. 1153-1181.

2. Hermance, C. E., "Solid Propellant Ignition Theories and Experiments," Contributing Chapter for AIAA Progress Series Volume Fundamentals of Combustion of Solid Propellants, edited by Kuo and Summerfield.

3. Kulkarni, A. K., Kumar, M., and Kuo, K. K., "Review of Solid Propellant Ignition Studies," AIAA paper 80-1210, also summarized in AIAA Journal, Vol. 20, Feb. 1982, p. 243.

4. Wills, J. E., Kumar, M., Kulkarni, A. K., and Kuo, K. K., "Abrupt Ignition of AP-Based Composite Propellant Under Severe Gas Loading Conditions," 1982 JANNAF Propulsion Systems Hazards Meeting, Apr. 1982.

5. Kumar, M. and Kuo, K. K., "Ignition of Solid Propellant at Crack Tip nder Rapid Pressurization," AIAA Journal, Vol. 18, Jul. 1980, pp. 825-833.

6. Kumar, M., Wills, J. E., Kulkarni, A. K., and Kuo, K. K., "Ignition of Composite Propellants in a Stagnation Region Under Rapid Pressure Loading," 19th Symposium (International) on Combustion, Aug. 1982, pp. 757-767.

7. Kumar, M., Wills, J. E., Kulkarni, A. K., and Kuo, K. K., "A Model for AP-Based Composite Propellant Ignition Including Gas-Phase and Subsurface Reactions," AIAA Paper No. 82-1109, presented at AIAA/SAE/ASME 18th Joint Propulsion Conference, June 21-23, 1982 (accepted for publication in AIAA Journal).

8. Kubota, N., "Survey of Rocket Propellants and Their Combustion Characters," Contributing Chapter for AIAA Progress Series Volume Fundamentals of Combustion of Solid Propellants, edited by Kuo and Summerfield.

9. Kubota, N., "Combustion Mechanisms of Nitramine Composite Propellants," 18th Symposium (International) on Combustion, 1981, pp. 187-194.

10. Wise, S. and Rochio, J. J., "Binder Requirements for Low Vulnerability Propellants," 18th JANNAF Combustion Meeting, Vol. 2, 1981, pp. 305-320.

11. Wise, S., Rochio, J. J., and Reeves, H. J., "The Ignitability of Composite Nitramine Propellants," 17th JANNAF Combustion Meeting, Nov. 1980, pp. 457-475.

12. DeLuca, L., Caveny, L. H., Ohlemiller, T. J., and Summerfield, M., "Radiative Ignition of Double base Propellants: I. Some Formulation Effects," AIAA Journal, Vol. 14, Jul. 1976, pp. 940-946.

13. DeLuca, L., Ohlemiller, T. J., Caveny, L. H., and Summerfield, M., "Radiative Ignition of Double Base Propellants: II. Pre-ignition Events and

Source Effects," AIAA Journal, Vol. 8, Aug. 1976, pp. 1111-1117.

14. Birk, A., and Caveny, L. H., "Ignition of Solid Propellants Under Transient Flow Conditions," 16th JANNAF Combustion Meeting, CPIA Publ. 308, 1979, pp. 514-540.

15. Ohlemiller, T. J. and Summerfield, C. E., "Gas Phase Ignition Theory of a Heterogeneous Solid Propellant," Combustion Science and Technology, Vol. 4, 1957, pp. 191-196.

16. Schroeder, M. A., "Critical Analysis of Nitramine Decomposition Results: Some Comments on Chemical Mechanisms," 16th JANNAF Combustion Meeting, CPIA Publication 308, Vol. II, Dec. 1979, pp. 17-34.

17. Schroeder, M. A., "Critical Analysis of Nitramine Decomposition Data: Activation Energies and Frequency Factors of RDX and HMX Decomposition," 17th JANNAF Combustion Meeting, CPIA Publ. 329, Vol. 2, Nov. 1980, pp. 493-508.

18. Schroeder, M. A., "Critical Analysis of Nitramine Decomposition Data: Product Distributions from HMX and RDX Decomposition," 18th JANNAF Combustion Meeting, CPIA Publ. 347, Vol. 2, Oct. 1981, pp. 395-411.

19. Boggs, T. L., "The Thermal Behavior of Cyclotrimethylenetrinitramine (RDX) and Cyclotetramethylene tetranitramine (HMX)," contributing chapter for AIAA Progress Series Volume, Fundamentals of Combustion of Solid Propellants, edited by Kuo and Summerfield.

20. McCarty, K. P., "HMX propellant Combustion Studies: Phase I, Literature Search and Data Assessment," AFRPL-TR-76-59, Dec. 1976.

21. Shaw, R. and Walker, F. E., "Estimated Kinetics and Thermochemistry of Some Initial Unimolecular Reactions in the Thermal Decomposition of 1, 3, 5, 7,-tetranitro-1, 3, 5, 7,-tetrazacycloctane in the Gas Phase," J. Phys. Chem., Vol. 81, 1977, p. 2572.

22. McMillen, D. F., Barket, J. R., Lewis, K. E., Trevor, P. L., and Golden, D. M., "Mechanisms of Nitramine Decomposition: Very low Pressure Pyrolysis of HMX and Dimethynitramine," SRI Project PYU5787, Jun. 1979.

23. Suryanarayana and R. J., Graybush, "Thermal Decomposition of 1, 3, 5, 7-tetranitro-1, 3, 5, 7-tetrazacyclooctane (HMX): A Mass Spectrometric Study of the Products from -HMX," Gr. X-S. 24-591, Proc. 39th Congress on Ind. Chem., Brussels, Belgium, 1966.

24. Karpowicw, R. J., and Brill, T. B., "The -transformation of HMX: Its Thermal Analysis and Relationship to Propellants," AIAA Journal, Vol. 20, No. 11, 1982, p. 2586.

25. Cosgrove, J. D., and Own, A. J., "The Thermal Decomposition of 1, 3, 5-Trinitrohexahydro 1, 3, 5-Triazine (RDX) Part I: The Products and Physical Parameters," Combustion and Flame, Vol. 22, 1974, p. 13.

26. Cosgrove, J. D., and Owen, A. J., "The Thermal Decomposition of 1, 3, 5-Trinitrohexahydro 1, 3, 5-Triazine (RDX) Part II: The Products and Physical Parameters," Combustion and Flame, Vol. 22, 1974, p. 19.

27. Goshgarian, B. B., "The Thermal Decomposition of Cyclotrimethylenetrunitramine (RDX) and Cyclotetramethylenetetranitramine (HMX)," AFRPL-TR-78-76, Oct. 1978, (AD-B032 275L).

28. BenReuven, M. and Caveny, L. H., "Nitramine Flame Chemistry and Deflagration Interpreted in Terms of a Flame Model," 15th AIAA Propulsion Conference, No. 79-1133, Jun. 1979.

29. BenReuven, M. and Summerfield, M., "Combustion of Nitramine Propellants," ARBRL-CR-00507, Mar. 1983.

30. Kubota, N., "Physicochemical Processes of HMX Propellant Combustion," 19th Symposium (International) on Combustion, 1982, pp. 777-785.

31. Drummond, L. J., "Shock Induced Reactions of Methane with Nitrous and Nitric Oxides," Bull. Chem. Soc. Japan, Vol. 42, Feb. 1969, pp. 285-289.

32. Siefert, J. G. and Kuo, K. K., "Experimental Observations of Crack Propagation in Burning Solid Propellants," 19th JANNAF Combustion Meeting, CPIA Publication No. 366, Vol. I, Oct. 1982, pp. 407-416.

33. Swanson, S. R., "An Experimental Study of Dynamic Crack Propagation in a Filled Rubber," 16th Ann. Meeting Soc. Eng. Sci., Northwestern University, September 5-7, 1979.

34. Gent, A. N. and Marteny, P., "The Effect of Strain Upon the Velocity of Sound and the Velocity of Free Retraction for Natural Rubber," Technical Report No. 16 to ONR, May 1982.

35. ABAQUS Finite Element Program, Version 3-21-81, Hibbitt, Karlson, and Sorensen, Inc.

36. Kuo, K. K. and Coates, G. R., "Review of Dynamic Burning of Solid Propellants in Gun and Rocket Propulsion Systems," 16th Symposium (International) on Combustion, 1177-1191 (1976).

DISTRIBUTION LIST

	No. Copies		No. Copies
Dr. L.V. Schmidt Assistant Secretary of the Navy (R,E, and S) Room 5E 731 Pentagon Washington, D.C. 20350	1	Dr. F. Roberto Code AFRPL MKPA Edwards AFB, CA 93523	1
Dr. A.L. Slafkosky Scientific Advisor Commandant of the Marine Corps Code RD-1 Washington, D.C. 20380	1	Dr. L.H. Caveny Air Force Office of Scientific Research Directorate of Aerospace Sciences Bolling Air Force Base Washington, D.C. 20332	1
Dr. Richard S. Miller Office of Naval Research Code 413 Arlington, VA 22217	10	Mr. Donald L. Ball Air Force Office of Scientific Research Directorate of Chemical Sciences Bolling Air Force Base Washington, D.C. 20332	1
Mr. David Siegel Office of Naval Research Code 260 Arlington, VA 22217	1	Dr. John S. Wilkes, Jr. FJSRL/NC USAF Academy, CO 80840	1
Dr. R.J. Marcus Office of Naval Research Western Office 1030 East Green Street Pasadena, CA 91106	1	Dr. R.L. Lou Aerojet Strategic Propulsion Co. P.O. Box 15699C Sacramento, CA 95813	1
Dr. Larry Peebles Office of Naval Research East Central Regional Office 666 Summer Street, Bldg. 114-D Boston, MA 02210	1	Dr. V.J. Keenan Anal-Syn Lab Inc. P.O. Box 547 Paoli, PA 19301	1
Dr. Phillip A. Miller Office of Naval Research San Francisco Area Office One Hallidie Plaza, Suite 601 San Francisco, CA 94102	1	Dr. Philip Howe Army Ballistic Research Labs ARRADCOM Code DRDAR-BLT Aberdeen Proving Ground, MD 21005	1
Mr. Otto K. Heiney AFATL - DLDL Elgin AFB, FL 32542	1	Mr. L.A. Watermeier Army Ballistic Research Labs ARRADCOM Code DRDAR-BLI Aberdeen Proving Ground, MD 21005	1
Mr. R. Geisler ATTN: MKP/MS24 AFRPL Edwards AFB, CA 93523	1	Dr. W.W. Wharton Attn: DRSMI-RKL Commander U.S. Army Missile Command Redstone Arsenal, AL 35898	1

DISTRIBUTION LIST

	No. Copies		No. Copies
Dr. R.G. Rhoades Commander Army Missile Command DRSMI-R Redstone Arsenal, AL 35898	1	Dr. E.H. Debutts Hercules Inc. Baccus Works P.O. Box 98 Magna, UT 84044	1
Dr. W.D. Stephens Atlantic Research Corp. Pine Ridge Plant 7511 Wellington Rd. Gainesville, VA 22065	1	Dr. James H. Thacher Hercules Inc. Magna Baccus Works P.O. Box 98 Magna, UT 84044	1
Dr. A.W. Barrows Ballistic Research Laboratory USA ARRADCOM DRDAR-BLP Aberdeen Proving Ground, MD 21005	1	Mr. Theordore M. Gilliland Johns Hopkins University APL Chemical Propulsion Info. Agency Johns Hopkins Road Laurel, MD 20810	1
Dr. C.M. Frey Chemical Systems Division P.O. Box 358 Sunnyvale, CA 94086	1	Dr. R. McGuire Lawrence Livermore Laboratory University of California Code L-324 Livermore, CA 94550	1
Professor F. Rodriguez Cornell University School of Chemical Engineering Olin Hall, Ithaca, N.Y. 14853	1	Dr. Jack Linsk Lockheed Missiles & Space Co. P.O. Box 504 Code Org. 83-10, Bldg. 154 Sunnyvale, CA 94088	1
Defense Technical Information Center DTIC-DDA-2 Cameron Station Alexandria, VA 22314	12	Dr. B.G. Craig Los Alamos National Lab P.O. Box 1663 NSP/DOD, MS-245 Los Alamos, NM 87545	1
Dr. Rocco C. Musso Hercules Aerospace Division Hercules Incorporated Alleghany Ballistic Lab P.O. Box 210 Washington, D.C. 21502	1	Dr. R.L. Rabie WX-2, MS-952 Los Alamos National Lab. P.O. Box 1663 Los Alamos NM 37545	1
Dr. Ronald L. Simmons Hercules Inc. Eglin AFATL/DLDL Eglin AFB, FL 32542	1	Dr. R. Rogers, WX-2 Los Alamos Scientific Lab. P.O. Box 1663 Los Alamos, NM 87545	1

DISTRIBUTION LIST

	No. Copies		No. Copies
Mr. R. Brown Naval Air Systems Command Code 330 Washington, D.C. 20361	1	Dr. J. Schnur Naval Research Lab. Code 6510 Washington, D.C. 20375	1
Dr. H. Rosenwasser Naval Air Systems Command AIR-310C Washington, D.C. 20360	1	Mr. R. Beauregard Naval Sea Systems Command SEA 64E Washington, D.C. 20362	1
Mr. B. Sobers Naval Air Systems Command Code 03P25 Washington, D.C. 20360	1	Mr. G. Edwards Naval Sea Systems Command Code 62R3 Washington, D.C. 20362	1
Dr. L.R. Rothstein Assistant Director Naval Explosives Dev. Engineering Dept. Naval Weapons Station Yorktown, VA 23691	1	Mr. John Boyle Materials Branch Naval Ship Engineering Center Philadelphia, PA 19112	1
Dr. Lionel Dickinson Naval Explosive Ordnance Disposal Tech. Center Code D Indian Head, MD 20640	1	Dr. H.G. Adolph Naval Surface Weapons Center Code R11 White Oak Silver Spring, MD 20910	1
Mr. C.L. Adams Naval Ordnance Station Code PM4 Indian Head, MD 20640	1	Dr. T.D. Austin Naval Surface Weapons Center Code R16 Indian Head, MD 20640	1
Mr. S. Mitchell Naval Ordnance Station Code 5253 Indian Head, MD 20640	1	Dr. T. Hall Code R-11 Naval Surface Weapons Center White Oak Laboratory Silver Spring, MD 20910	1
Dr. William Tolles Dean of Research Naval Postgraduate School Monterey, CA 93940	1	Mr. G.L. Mackenzie Naval Surface Weapons Center Code R101 Indian Head, MD 20640	1
Naval Research Lab. Code 6100 Washington, D.C. 20375	1	Dr. K.F. Mueller Naval Surface Weapons Center Code R11 White Oak Silver Spring, MD 20910	1

DISTRIBUTION LIST

	No. Copies		No. Copies
Mr. J. Murrin Naval Sea Systems Command Code 62R2 Washington, D.C. 20362	1	Dr. A. Nielsen Naval Weapons Center Code 385 China Lake, CA 93555	1
Dr. D.J. Pastine Naval Surface Weapons Cneter Code RC4 White Oak Silver Spring, MD 20910	1	Dr. R. Reed, Jr. Naval Weapons Center Code 388 China Lake, CA 93555	1
Mr. L. Roslund Naval Surface Weapons Center Code R122 White Oak, Silver Spring MD 20910	1	Dr. L. Smith Naval Weapons Center Code 3205 China Lake, CA 93555	1
Mr. M. Stosz Naval Surface Weapons Center Code R121 White Oak Silver Spring, MD 20910	1	Dr. B. Douda Naval Weapons Support Center Code 5042 Crane, Indiana 47522	1
Dr. E. Zimmet Naval Surface Weapons Center Code R13 White Oak Silver Spring, MD 20910	1	Dr. A. Faulstich Chief of Naval Technology MAT Code 0716 Washington, D.C. 20360	1
Dr. D. R. Derr Naval Weapons Center Code 388 China Lake, CA 93555	1	LCDR J. Walker Chief of Naval Material Office of Naval Technology MAT, Code 0712 Washington, D.C. 20360	1
Mr. Lee N. Gilbert Naval Weapons Center Code 3205 China Lake, CA 93555	1	Mr. Joe McCartney Naval Ocean Systems Center San Diego, CA 92152	1
Dr. E. Martin Naval Weapons Center Code 3853 China Lake, CA 93555	1	Dr. S. Yamamoto Marine Sciences Division Naval Ocean Systems Center San Diego, CA 91232	1
Mr. R. McCarten Naval Weapons Center Code 3272 China Lake, CA 93555	1	Dr. G. Bosmajian Applied Chemistry Division Naval Ship Research & Development Center Annapolis, MD 21401	1
		Dr. H. Shuey Rohn and Haas Company Huntsville, Alabama 35801	1

DISTRIBUTION LIST

	No. Copies		No. Copies
Dr. J.F. Kincaid Strategic Systems Project Office Department of the Navy Room 901 Washington, D.C. 20376	1	Dr. C.W. Vriesen Thiokol Elkton Division P.O. Box 241 Elkton, MD 21921	1
Strategic Systems Project Office Propulsion Unit Code SP2731 Department of the Navy Wahsington, D.C. 20376	1	Dr. J.C. Hinshaw Thiokol Wasatch Division P.O. Box 524 Brigham City, Utah 83402	1
Mr. E. L. Throckmorton Strategic Systems Project Office Department of the Navy Room 1048 Wash:ngton, D.C. 20376	1	U.S. Army Research Office Chemical & Biological Sciences Division P.O. Box 12211 Research Triangle Park NC 27709	1
Dr. D.A. Flanigan Thiokol Huntsville Division Huntsville, Alabama 35807	1	Dr. R.F. Walker USA ARRADCOM DRDAR-LCE Dover, NJ 07801	1
Mr. G.F. Mangum Thiokol Corporation Huntsville Division Huntsville, Alabama 35807	1	Dr. T. Sinden Munitions Directorate Propellants and Explosives Defence Equipment Staff British Embassy 3100 Massachusetts Ave. Washington, D.C. 20008	1
Mr. E.S. Sutton Thiokol Corporation Elkton Division P.O. Box 241 Elkton, MD 21921	1	LTC B. Loving AFROL/LK Edwards AFB, CA 93523	1
Dr. G. Thompson Thiokol Wasatch Division MS 240 P.O. Box 524 Brigham City, UT 84302	1	Professor Alan N. Gent Institute of Polymer Science University of Akron Akron, OH 44325	1
Dr. T.F. Davidson Technical Director Thiokol Corporation Government Systems Group P.O. Box 9258 Odgen, Utah 84409	1	Mr. J.M. Frankle Army Ballistic Research Labs ARRADCOM Code DRDAR-BLI Aberdeen Proving Ground, MD 21005	1

DISTRIBUTION LIST

No. Copies   No. Copies

Dr. Ingo W. May   1   Dr. J. P. Marshall   1
Army Ballistic Research Labs   Dept. 52-35, Bldg. 204/2
ARRADCOM   Lockheed Missile & Space Co.
Code DRDAR-BLI   3251 Hanover Street
Aberdeen Proving Ground, MD 21005   Palo Alto, CA 94304

Professor N.W. Tschoegl   1   Ms. Joan L. Janney   1
California Institute of Tech   Los Alamos National Lab
Dept. of Chemical Engineering   Mail Stop 920
Pasadena, CA 91125   Los Alamos, NM 87545

Professor M.D. Nicol   1   Dr. J. M. Walsh   1
University of California   Los Alamos Scientific Lab
Dept. of Chemistry   Los Alamos, NM 87545
405 Hilgard Avenue
Los Angeles, CA 90024   Professor R. W. Armstrong   1
                                                Univ. of Maryland
Professor A. G. Evans   1   Department of Mechanical Eng.
University of California   College Park, MD 20742
Berkeley, CA 94720
                                                Prof. Richard A. Reinhardt   1
Professor T. Litovitz   1   Naval Postgraduate School
Catholic Univ. of America   Physics & Chemistry Dept.
Physics Department   Monterey, CA 93940
520 Michigan Ave., N.E.
Washington, D.C. 20017   Dr. R. Bernecker   1
                                                Naval Surface Weapons Center
Professor W. G. Knauss   1   Code R13
Graduate Aeronautical Lab   White Oak, Silver Spring, MD 20910
California Institute of Tech.
Pasadena, CA 91125   Dr. M. J. Kamlet   1
                                                Naval Surface Weapons Center
Professor Edward Price   1   Code R11
Georgia Institute of Tech.   White Oak, Silver Spring, MD 20910
School of Aerospace Engin.
Atlanta, Georgia 30332   Professor J. D. Achenbach   1
                                                Northwestern University
Dr. Kenneth O. Hartman   1   Dept. of Civil Engineering
Hercules Aerospace Division   Evanston, IL 60201
Hercules Incorporated
P.O. Box 210   Dr. N. L. Basdekas   1
Cumberland, MD 21502   Office of Naval Research
                                                Mechanics Program, Code 432
Dr. Thor L. Smith   1   Arlington, VA 22217
IBM Research Lab
D42.282   Professor Kenneth Kuo   1
San Jose, CA 95193   Pennsylvania State Univ.
                                                Dept. of Mechanical Engineering
                                                University Park, PA 16802

DISTRIBUTION LIST

	No. Copies		No. Copies

Dr. S. Sheffield   1
Sandia Laboratories
Division 2513
P.O. Box 5800
Albuquerque, NM 87185

Dr. M. Farber   1
Space Sciences, Inc.
135 Maple Avenue
Monrovia, CA 91016

Dr. Y. M. Gupta   1
SRI International
333 Ravenswood AVenue
Menlo Park, CA 94025

Mr. M. Hill   1
SRI International
333 Ravenswood Avenue
Menlo Park, CA 94025

Professor Richard A. Schapery   1
Texas A&M Univ.
Dept of Civil Engineering
College Station, TX 77843

Dr. Stephen Swanson   1
Univ. of Utah
Dept. of Mech. & Industrial
    Engineering
MEB 3008
Salt Lake City, UT 84112

Mr. J. D. Byrd   1
Thiokol Corp. Huntsville
Huntsville Div.
Huntsville, AL 35807

Professor G. D. Duvall   1
Washington State University
Dept. of Physics
Pullman, WA 99163

Prof. T. Dickinson   1
Washington State University
Dept. of Physics
Pullman, WA 99163